



## Article

# Gas-Solid Flow in a Fluidized-Particle Tubular Solar Receiver: Off-Sun Experimental Flow Regimes Characterization

Ronny Gueguen <sup>1</sup>, Guillaume Sahuquet <sup>1</sup>, Samuel Mer <sup>2</sup>, Adrien Toutant <sup>2</sup>, Françoise Bataille <sup>2</sup> and Gilles Flamant <sup>1,\*</sup>

<sup>1</sup> Processes, Materials and Solar Energy Laboratory, PROMES-CNRS, 7, Rue du Four Solaire, 66120 Font-Romeu, France; ronny.gueguen@promes.cnrs.fr (R.G.); guillaume.sahuquet@promes.cnrs.fr (G.S.)

<sup>2</sup> PROMES-CNRS Laboratory, Engineering Science Department, University of Perpignan (UPVD), Tecnosud, Rambla de la Thermodynamique, 66100 Perpignan, France; samuel.mer@univ-perp.fr (S.M.); adrien.toutant@univ-perp.fr (A.T.); francoise.bataille@promes.cnrs.fr (F.B.)

\* Correspondence: gilles.flamant@promes.cnrs.fr

**Abstract:** The fluidized particle-in-tube solar receiver concept is promoted as an attractive solution for heating particles at high temperature in the context of the next generation of solar power tower. Similar to most existing central solar receivers, the irradiated part of the system, the absorber, is composed of tubes in which circulate the fluidized particles. In this concept, the bottom tip of the tubes is immersed in a fluidized bed generated in a vessel named the dispenser. A secondary air injection, called aeration, is added at the bottom of the tube to stabilize the flow. Contrary to risers, the particle mass flow rate is controlled by a combination of the overpressure in the dispenser and the aeration air velocity in the tube. This is an originality of the system that justifies a specific study of the fluidization regimes in a wide range of operating parameters. Moreover, due to the high value of the aspect ratio, the particle flow structure varies along the tube. Experiments were conducted with Geldart Group A particles at ambient temperature with a 0.045 m internal diameter and 3 m long tube. Various temporal pressure signal processing methods, applied in the case of classical risers, are applied. Over a short acquisition time, a cross-reference of the results is necessary to identify and characterize the fluidization regimes. Bubbling, slugging, turbulent and fast fluidization regimes are encountered and the two operation modes, without and with particle circulation, are compared.

**Keywords:** fluidization regimes; dense particle suspension; particle-in-tube solar receivers; hydrodynamics of gas-solid flow; upward circulation; pressure signal processing



**Citation:** Gueguen, R.; Sahuquet, G.; Mer, S.; Toutant, A.; Bataille, F.; Flamant, G. Gas-Solid Flow in a Fluidized-Particle Tubular Solar Receiver: Off-Sun Experimental Flow Regimes Characterization. *Energies* **2021**, *14*, 7392. <https://doi.org/10.3390/en14217392>

Academic Editors: Hairui Yang, Franz Winter, Artur Blaszcuk and Rafal Kobylecki

Received: 9 September 2021

Accepted: 2 November 2021

Published: 5 November 2021

**Publisher's Note:** MDPI stays neutral with regard to jurisdictional claims in published maps and institutional affiliations.



**Copyright:** © 2021 by the authors. Licensee MDPI, Basel, Switzerland. This article is an open access article distributed under the terms and conditions of the Creative Commons Attribution (CC BY) license (<https://creativecommons.org/licenses/by/4.0/>).

## 1. Introduction

Concentrated solar power (CSP) plants convert solar radiation into electricity using a thermodynamic cycle. In solar towers, a heliostat field focuses the solar irradiation onto a solar receiver located at the top of the tower, in which a heat transfer fluid (HTF) absorbs the heat from the concentrated solar power. The HTF circulates through a heat exchanger to transfer the heat either to a storage tank or to another fluid like air or steam. This working fluid powers a turbine that produces electricity. The stored part is used to supply electricity on demand. The commonly used HTF is the solar salt (KNO<sub>3</sub>–NaNO<sub>3</sub> eutectic), which is efficient because it can be used as HTF and storage medium but is limited in minimum and maximum operating temperatures because of solidification ( $\approx 220$  °C) and chemical decomposition (565 °C) respectively [1,2].

In order to overcome these issues, three laboratories are developing different solar receiver concepts based on the utilization of particles as heat transfer medium. The Sandia National Laboratory (United States) and the German Aerospace Center (Germany) study the falling particle and the centrifugal receivers, respectively [3,4]. The CNRS (France) has, since 2010, developed a receiver concept based on upward forced circulation of a fluidized particle through long irradiated tubes [5]. In such a receiver, the tubes are immersed in

a vessel called the dispenser that acts as a feeder tank. In the dispenser, the particles are fluidized and an upward particle flow in the tubes is obtained by applying a pressure in the freeboard of the dispenser. This type of flow differs greatly from risers, widely studied in the literature, since it is not only the velocity of the carrier phase (i.e., air) that generates the upward flow of particles but a combination of the latter and a pressure gradient between the dispenser and the collector. As a result, the solid volume fraction of the generated upward flow varies in a wide range. This concept, more detailed in Section 2.1, presents several technological benefits. First, the use of a tubular receiver that is similar to those used with molten salts. Second, particles are not limited to a particular working temperature range, contrary to molten salts. Third, the same medium can be used as HTF and storage material. At large scale and high temperature ( $>700$  °C), the use of a cavity is needed to improve thermal efficiency by reducing thermal losses [6]. Furthermore, high operation temperatures open the route for high-temperature thermodynamic cycles that improve the heat-to-electricity efficiency [7]. Additional advantages are economic and environmental. Depending on the chosen particles, it can significantly reduce the costs of the HTF and storage medium: around 150–200 \$/ton, i.e., significantly less than molten salts [8]. Finally, the use of mineral particles allows a reduction in the environmental footprint of the power plant [9].

Several papers have been published in the framework of the Concentrated Solar Power in Particles (CSP2) and the Next-CSP European projects [10,11]. The studied configurations focus on one or several tubes, with irradiated heights of 1 m and with aeration flow rates and particles mass fluxes up to  $0.7 \text{ m}^3/\text{h}$  and  $110 \text{ kg}/\text{m}^2\text{s}$  respectively [12–15]. Wall-to-fluidized bed heat transfer coefficients up to  $1200 \text{ W}/\text{m}^2\text{K}$  have been observed experimentally with finned tubes. These articles emphasize that the thermal performances of the solar receiver are strongly correlated to the hydrodynamics of the two-phase flow. Two transitions of regime have been identified in this kind of tube: from bubbling to wall slugging and then to axisymmetric slugging [16,17]. Since the formation of axisymmetric slugs result in a significant decrease of the wall-to-bed heat transfer because of a reduction of particle mixing, the identification of the fluidization regime is critical for solar applications [18,19].

However, those previous experimental studies focus mainly on the proof of concept and on global understanding of the heat transfer under solar irradiation [12–15]. Experimental set-ups were richly instrumented in thermocouples but poorly in terms of pressure probes along the receiver, which prevented the identification of the different fluidization regimes. In more recent studies, fluidization regimes were analysed by means of a high-speed camera [16,19]. However, in [19] the authors studied only a particle non-circulating configuration. The use of temporal pressure signals, which is a powerful tool to identify the fluidization regimes in the tubes of the receiver is not discussed in these papers. From the previous point of view, an originality of this work lies in the use of cross-diagnostics with the different methods in order to reduce the acquisition time needed to detect the flow regime (classically of the order of magnitude of an hour). Furthermore, the previous studies cover a limited range of the aeration flow rate, which limits the spectrum of observable fluidization regimes to bubbling and slugging. Increasing this flow rate could lead to a turbulent fluidization regime that is characterized by both a decrease of the particles volume fraction and a strong increase of the particles mixing [20]. Such regime could help to improve the heat transfer, as predicted by [16]. Such simple reasoning motivates a broadening of the range of the aeration flow rate, in order to improve the internal mixing of the suspension. Under on-sun conditions, it could also improve the wall-to-bed heat transfer coefficient and thus the receiver efficiency. Moreover, a comparison of flow regimes between circulating and non-circulating operation conditions is another originality of this paper.

This paper aims to compare several analysis methods of temporal pressure signals to identify and characterize the different fluidization regimes in an upward, dense, gas-solid flow inside a tube with a large aspect ratio (height/internal diameter  $> 80$ ), at ambient

temperature. A mock-up was set up to study the evolution of the flow structure using pressure measurements through a wide range of experimental parameters, in particular the gas velocity, which enables the turbulent fluidization regime to be reached. The experimental set-up is presented first and then the different methods used to analyse the pressure signals. The fluidization regimes in the tube are then identified on the basis of temporal pressure signal-processing methods.

## 2. Experimental Set-Up

### 2.1. Cold Mock-Up

The cold mock-up is presented in Figure 1. It is composed of a dispenser (section  $S_{disp}$  of  $0.571 \text{ m}^2$ ), in which the particles are fluidized with an air flow rate,  $\dot{q}_f$ , through a porous metal plate distributor (bronze). The latter ensures a homogenous distribution of the air flow in the dispenser.  $\dot{q}_f$  is kept constant at  $16.8 \text{ sm}^3/\text{h}$  to obtain a homogeneous freely bubbling regime in the dispenser. This corresponds to a fluidization velocity  $U_f$  of  $0.97 \text{ cm/s}$ , i.e.,  $1.7 * U_{mb}$ , where  $U_{mb}$  stands for the minimum bubbling velocity of the particles (cf. Section 2.2). A glass tube, of a total height  $H_t = 3.63 \text{ m}$  and an internal diameter (I.D.)  $D_t = 45 \text{ mm}$ , is immersed into the fluidized bed up to  $7 \text{ cm}$  above the porous distributor.

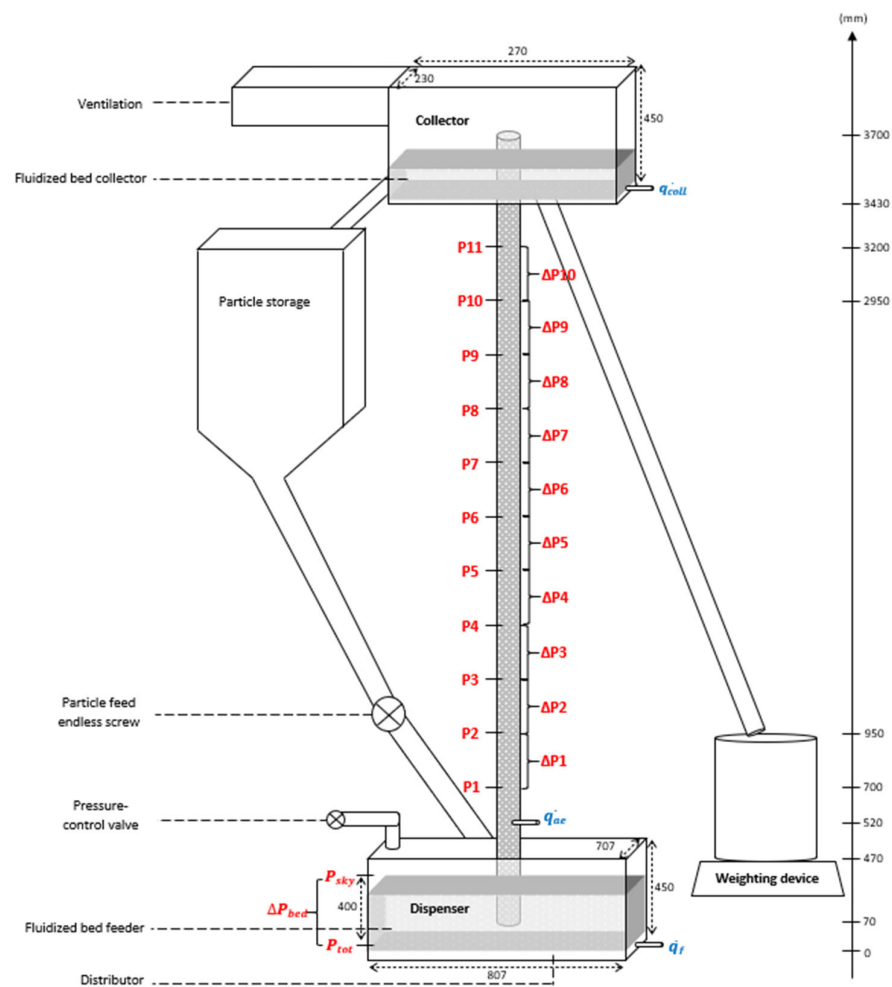


**Figure 1.** Schematic description of the cold mock-up with instrumentation details.

A pressure-control valve enables control of the overpressure in the freeboard of the dispenser. Increasing the freeboard pressure results in the gas-particle suspension flowing upward in the tube and reaching the collector at atmospheric pressure. Particles are also fluidized in the collector to ease the particle discharge. The difference between the total

pressure of the dispenser i.e., the sum of the freeboard pressure and the pressure drop through the dispenser and the atmospheric pressure is the driving pressure of the system,  $P_{tot}$ .

A weighting scale is placed at the tube discharge to measure the time-dependent particle mass flow rate  $\dot{m}_p$ . A storage tank is connected to the dispenser by a rotary valve, which feeds the dispenser with particles to keep the particle mass in the dispenser and thus the total pressure approximately constant during a test.

In order to stabilize the flow, a secondary air flow rate  $\dot{q}_{ae}$ , called “aeration”, is injected through a nozzle of 1.5 mm I.D. at the bottom of the tube (0.52 m above the porous distributor) [15]. The tube is equipped with eleven pressure sockets regularly spaced by 25 cm, the first probe being located 18 cm above the aeration injection. These sockets are connected to differential or relative pressure sensors depending on the targeted measurements. The measurement ranges and response times of the sensors and flow meters fit the experimental requirements, as presented in Appendix A. They are connected to data acquisition systems.

The control parameters of the facility are the following:

- The aeration air flow rate in the tube  $\dot{q}_{ae}$  ranges from 0.4 to 2.5  $\text{m}^3/\text{h}$ . The superficial air velocity in the tube  $U_{air}$  is the sum of the superficial velocities in the dispenser and the tube,  $U_f$  and  $U_{ae}$  respectively, and ranges from 0.01 to 0.54 m/s.
- The driving pressure of the system  $P_{tot}$ , i.e., the relative total pressure in the dispenser, varies up to 413 mbar for the tests considered in this paper. Combined with the aeration, it allows the suspension to reach a given height in the tube or to flow at a given mass flow rate outside the tube.
- The level of the suspension in the tube  $H_{bed}$  varies but is limited by the tube height  $H_t = 3.18$  m above the aeration injection.
- The particles mass flux  $G_p$ , i.e., the solid mass flow rate  $\dot{m}_p$  divided by the section of the tube  $S_t = 0.0016$   $\text{m}^2$ , is determined by linear regression of the particle mass weight recorded by the weighting scale during an acquisition. It varies during the test campaign up to 122  $\text{kg}/\text{m}^2\text{s}$  (698  $\text{kg}/\text{h}$ ).

## 2.2. Particles

Olivine particles are used. They were selected for their good thermal, mechanical and fluidization properties [9]. Both the particle size distribution and their characteristic fluidization velocities have been measured. The properties of the olivine sample are summarized in Table 1.

**Table 1.** Properties of the olivine sample.

	$d_{SV}$ ( $\mu\text{m}$ )	$d_V$ ( $\mu\text{m}$ )	$\varphi$	$\sigma$	$Ar$
Particle size	61 $\mu\text{m}$	81 $\mu\text{m}$	75%	59.6%	21
	$U_{mf}$ (cm/s)	$U_{mb}$ (cm/s)	$U_t$ (m/s)	$U_k$ (m/s)	
Velocities	$0.42 \pm 0.03$	$0.57 \pm 0.04$	$0.40 \pm 0.04$	$0.49 \pm 0.04$	

The particle size distribution of the olivine sample (Figure 2) has been determined by laser diffraction using a Malvern Mastersizer 3000 granulometer. The Sauter mean diameter  $d_{sv}$  is estimated at 61  $\mu\text{m}$  [18,21]. This value is relatively low compared with the peak of the distribution (at 79  $\mu\text{m}$ ) because the  $d_{sv}$  takes into account the presence of fine particles. The spread of the size distribution is calculated as  $\sigma = (d_{90} - d_{10}) / (2d_{50}) = 59.6\%$ , where  $d_X$  is the diameter corresponding to the X% value on the cumulated distribution (dashed curve in Figure 2). The volume diameter  $d_v$  is estimated as 81  $\mu\text{m}$  and the mean sphericity of the sample is  $\varphi = d_{sv} / d_v = 75\%$ . With a particle density  $\rho_p$  of 3300  $\text{kg}/\text{m}^3$  and a calculated Archimedes dimensionless number of 21 (calculated considering the viscosity of the air at atmospheric pressure and 20 °C of  $1.85 \times 10^{-5}$  Pa.s), these data confirm that the olivine sample belongs to group A of the Geldart classification [22].

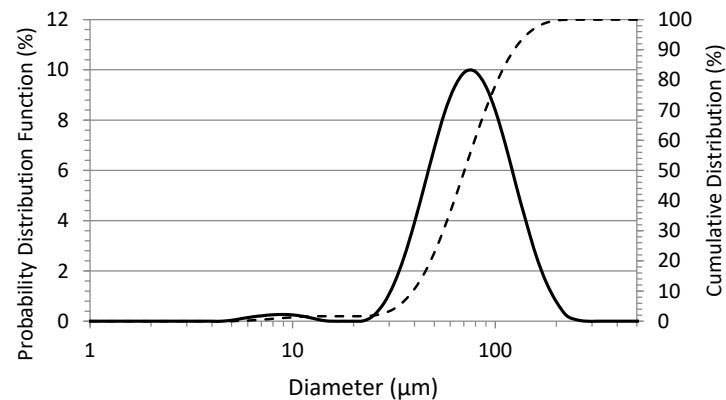


**Figure 2.** Particle size distribution, relative (solid curve) and cumulative (dashed curve).

The particles concentration for the fixed bed was estimated at  $0.48 \pm 0.02$  by weighing a known occupied volume. The characteristic fluidization velocities have been measured in a fluidization column of 9 cm I.D., as plotted in Figure 3. The minimum fluidization velocity  $U_{mf}$  is determined by the pressure drop versus air velocity (Figure 3a), at the intersection of the curves relative to the fixed bed and the fluidized bed at decreasing air velocity to avoid channelling [23,24]. The minimum bubbling velocity  $U_{mb}$  is identified in Figure 3a at increasing air velocity when the pressure drop through the fluidized bed dramatically decreases, which is representative of the first bubbles erupting at the bed surface [25]. The calculated values are respectively 0.42 and 0.57 cm/s, which are in good agreement with the correlations in the literature for group A particles [24,26]. The small difference between  $U_{mf}$  and  $U_{mb}$  is due to the amount of fine particles in the sample.

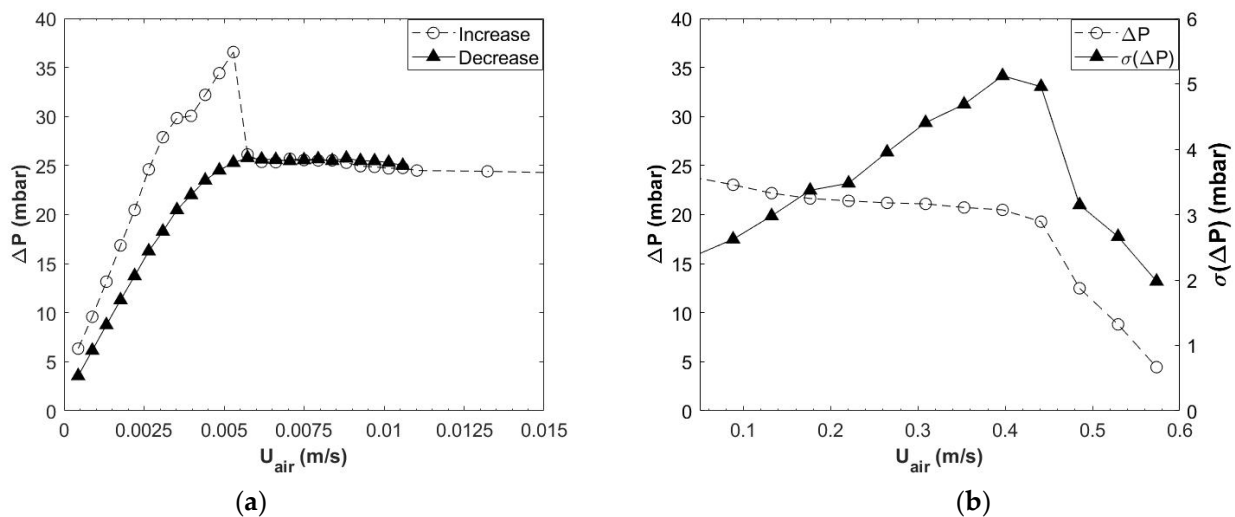


**Figure 3.** Determination of the characteristic fluidization velocities by common pressure drop versus the superficial air velocity (a) for low velocities, to identify the onset of fluidization and of bubbling, and (b) for high velocities, to identify the onset of the turbulent and the fast fluidization regimes.

Figure 3b shows the minimum velocities that delimit the turbulent fluidization regime,  $U_t$  and  $U_k$ .  $U_t$  is identified at 0.40 m/s when the pressure fluctuations reach a maximum [27].  $U_k$  corresponds to the terminal velocity, where the fast fluidization regime occurs. In the standard column, the particles are entrained outside of the vessel, characterized by a strong diminution of the measured pressure drop and a level-off of the pressure fluctuations if the bed is not fed [27,28].  $U_k$  was thus identified at 0.49 m/s. According to [28], the fast fluidization is characterized by a phase inversion: there are no more void but particles structures (i.e., clusters) inside the suspension, entrained upward at high velocities. This



is discussed in Section 4. The  $U_t$  and  $U_k$  velocities are very close because the turbulent regime zone is very narrow with the particles used, as predicted by [29].

### 3. Scientific Background

The methods presented in this section are classically used in the literature to study fluidized beds and fluidization regimes. However, an originality of this work lies in the use of cross-diagnostics with the different methods in order to reduce the acquisition time needed to detect the flow regime (classically of the order of magnitude of an hour). This work will allow, from an application point of view, the detection of the flow regimes in quasi-real time.

#### 3.1. Solid Volume Fraction Analysis

The dimensionless solid volume fraction  $\alpha_p$  is the proportion of the volume occupied by the particles. It is the opposite of the porosity,  $\alpha_p = 1 - \varepsilon$ , and it is determined from pressure drop measurements. The evolution of this quantity with the tube height is an indicator to identify some fluidization regimes. This point is discussed in Section 4. The pressure drop over a height  $H$  can be decomposed into a sum of three contributions, as explained in [30]:

- A pressure drop due to the energy used to accelerate the particles until the particle velocity,  $\Delta P_{acc} = G_p U_p$ .
- A pressure drop due to the effective weight of the suspension,  $\Delta P_p = \alpha_p (\rho_p - \rho_{air}) g H$ .
- A pressure drop due to the friction against the tube walls,  $\Delta P_{fr} = (\alpha_p 3 C_D \rho_{air} H / (4 d_{sv})) (U_{air} - U_p)^2$ , with  $C_D$  the friction coefficient calculated at 0.925 by the method described by [31].

In our experiments, the total pressure losses due to particle acceleration and wall friction represent less than 3% of the measured pressure drop, which is of the order of magnitude of the observed pressure fluctuations. Those pressure drops are thus negligible, as shown in [32], and the pressure drop in the tube can be expressed in terms of the suspension's effective weight only. This leads to the averaged local solid volume fraction in a tube volume between two pressure sockets Equation (1), at the average height  $\bar{h}_i = \frac{h_{i+1} + h_i}{2}$ , and with  $\Delta h_i = h_{i+1} - h_i = 25$  cm the distance between two sockets.

$$\alpha_i(\bar{h}_i) = \frac{\Delta \bar{P}_i}{(\rho_p - \rho_{air}) g \Delta h_i} \quad (1)$$

In Equation (1),  $\Delta \bar{P}_i$  is the mean value of the  $i^{\text{th}}$  differential pressure signal, calculated along the entire time of an acquisition. A typical differential pressure signal is presented in Figure 4, with the mean value in red dashed line. The sensors measurement error is 0.05 mbar and is thus negligible compared with the pressure fluctuations around the mean value. These fluctuations are represented by the standard deviation of the signal (black dashed lines in Figure 4), which is directly related to the fluidization regime. The overall solid fraction along the total bed height is calculated as the average of the  $n$  measured local solid fractions along the tube height,  $\alpha_h = \frac{1}{n} \sum_{i=1}^n \alpha_i$ .

#### 3.2. Temporal Analyses

Pressure measurements are used in risers to study the hydrodynamics of the suspension. In fact, since an isolated structure (void or particles) moving in front of a pressure socket causes positive pressure at its top and a suction at its wake, the recorded temporal pressure signals result in a succession of upper and lower peaks [33,34]. These signals can hence be analysed in the time or frequency domains to identify the associated fluidization regimes [35–38]. Thus, the same methodology is applied with the particle-in-tube solar receiver concept studied in this paper. A succession of both an upper and a lower peak above and below the mean value of the signal materializes the passage of a slug or a cluster

of particles, while noisy peaks that do not cross the mean value are related to the passage of smaller structures, i.e., small bubbles or particle aggregates [36].

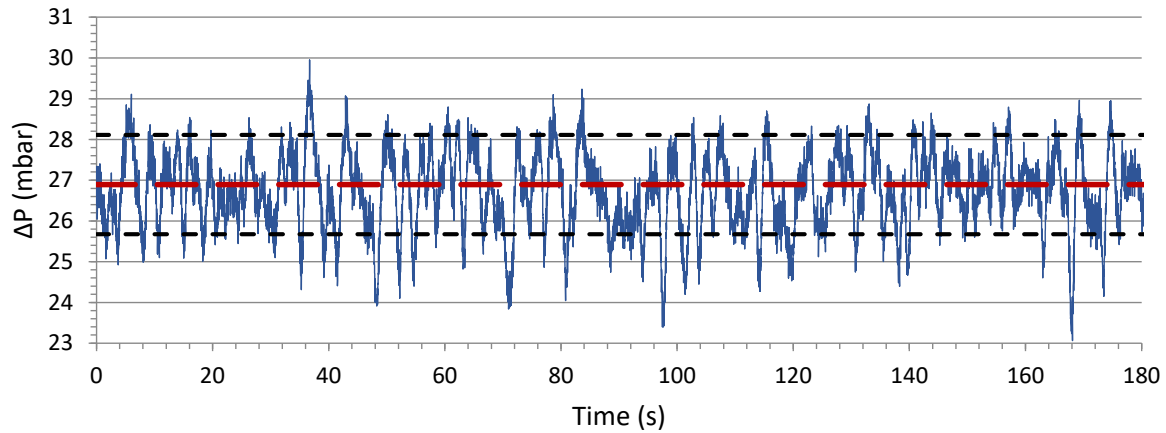


**Figure 4.** Example of a temporal differential pressure signal during a test. The dashed red line indicates the mean value of the signal, and the black ones correspond to the associated standard deviation, i.e., the fluctuations.

### 3.2.1. The Cross-Correlation

The marked peaks highlight a typical structure (here a void) propagation in the tube. Then, considering two pressure signals at successive positions in the tube,  $P_i(t)$  and  $P_{i+1}(t)$ , with  $P_i$  the lower position, the calculation of the cross-correlation function  $R_{i,i+1}$  enables us to determine the time lag  $\tau$  and apply it to  $P_{i+1}$ , and so maximizing its correlation with  $P_i$ . The cross-correlation function is calculated over a time window made of the  $N_{acq}$  acquisition point Equation (2) [36,37].

$$R_{i,i+1}(k) = \frac{1}{N_{acq} - k} \sum_{n=1}^{N_{acq}-k} P_i(n)P_{i+1}(n+k) \quad (2)$$

When two signals are correlated, the  $R_{i,i+1}$  function is maximal for the time lag  $\tau_m$ , which corresponds to the time taken by the structure to flow up between the two pressure sockets. In Equation (2), this time lag is related to a numerical lag  $k$  with the acquisition frequency  $f_{acq}$ . Knowing the distance between these positions in the tube  $\Delta h$ , the time lag can be related to the upward velocity of the perturbation at the examined level,  $U_{v,i}(\bar{h}_i) = \Delta h / \tau_{m,i}$ . The accuracy of this method to identify the fluidization regimes is discussed in Section 4.

### 3.2.2. The Coherence Analysis

The frequency of perturbation, i.e., the number of perturbations moving in front of a pressure probe per second, could be calculated by counting the number of peak characteristics in a pressure signal and dividing it by the acquisition duration. Such an approach is however limited by the difficulty in identifying the characteristic peaks. The coherence analysis proposed by [38] gives a mathematical tool to extract such frequencies from the measurements. A Fourier transform is applied to the signal  $P_i(t)$  to calculate its power spectral density (PSD)  $\phi_{ii}$ , Equation (3). In this equation,  $F_i(f)$  represents the fast Fourier transform (FFT) of  $P_i(t)$ . In order to smooth the obtained spectrum by reducing noise and highlight the relevant frequencies, the pressure signal is decomposed into  $M$  groups. The FFT is calculated for each group, and the sub-spectra are averaged to give the final PSD. This is denoted by the brackets in Equation (3).

$$\phi_{ii}(f) = \frac{1}{N} F_i(f) F_i^*(f) \quad (3)$$

$$\phi_{0i}(f) = \frac{1}{N} F_i(f) F_0^*(f) \quad (4)$$

In such complex flows, there are many noisy frequencies in the PSD function. These frequencies correspond to pressure waves associated with the experimental device, freely bubbling regime in the dispenser, fluctuations of the suspension surface or even to transient regimes. Some of these phenomena cause significant pressure fluctuations on the temporal signal. In the frequency domain, it means that the magnitudes associated to their frequencies are important and can hinder the identification of the targeted frequencies. To reduce the impact of these noisy frequencies, the cross power spectral density (CPSD)  $\phi_{0i}$  between the  $i^{\text{th}}$  pressure signal and a chosen reference, denoted by the “0” subscript, is also calculated Equation (4). Then, if the two pressure signals are coherent for one frequency, the CPSD function is maximum. Authors defined the coherence term  $\gamma_{0i}^2(f) = \Phi_{0i} \Phi_{0i}^* / (\Phi_{00} \Phi_{ii})$  to normalize this quantity [38]. It results in decreasing the influence of common frequencies, and the incoherent part of the studied pressure signal  $IOP_{0i}$  is then representative of the local phenomena, i.e., the local perturbations Equation (5). The dominant frequency of this new signal hence represents the perturbation frequency at the sensor height.

$$IOP_{0i}(f) = (1 - \gamma_{0i}^2(f)) * \phi_{ii}(f) \quad (5)$$

In the literature, some authors combine a huge number of short acquisitions at high frequency, to smooth the obtained spectra and identify the frequencies due to the fluidization regime [36]. However, the acquisition time is limited by the capacity of the particle storage tank in our experiments. Thus, the parameters of the frequency treatment need to be optimized by considering this constraint to highlight the relevant frequencies. The frequencies of studied voids being of the order of 1 Hz or less, an acquisition frequency of 20 Hz is pertinent [17–19]. Furthermore, according to [36], 16 groups of 1024 points each is enough to characterize bubbles. To characterize slugs and, more globally, perturbations of lower frequencies than bubbles, four groups of 1024 points each is adapted. This corresponds to 205 s of acquisition duration. Results associated with this method are presented in the following section.

## 4. Results

### 4.1. Experimental Parameters of the Compared Acquisitions

Seven aeration flow rates have been tested, from 0.4 to 2.5  $\text{sm}^3/\text{h}$ . For each flow rate, three tests have been recorded for different flow configurations: without particle circulation and the height of the suspension in the tube around 2 m above the aeration injection, and with circulation, for two particle mass fluxes,  $G_p \approx 50$  and  $100 \text{ kg}/\text{m}^2\text{s}$ . The operating parameters associated with these tests are presented in Table 2.

The superficial air velocity increases along the tube height because of the pressure decrease, as shown in Figure 5 for three aeration flow rates. For a given air flow rate, the plots are very similar with and without particles circulation. Thus, only tests without circulation are presented for the sake of clarity. The transition velocities, which mark the onset and the offset of the turbulent regime, respectively  $U_t$  and  $U_k$  (see Section 2.2), are presented in Figure 5 with dashed lines. Several fluidization regimes should be observed over the tests. The tests with 0.8  $\text{sm}^3/\text{h}$  aeration flow rate should be in the slugging regime, and those with 2.5  $\text{sm}^3/\text{h}$ , in the fast fluidization regime. Tests with intermediate flow rates could be transitional between these regimes because the air velocity exceeds the limit of  $U_t$  along the tube height.



**Table 2.** Operating parameters of the experimental acquisitions.

Aeration Flow Rate $q'_{ae}$ (sm <sup>3</sup> /h)	Tests without Circulation, $H_{bed}$ around 2 m	Tests with Circulation, $G_p$ around 50 kg/m <sup>2</sup> s	Tests with Circulation, $G_p$ around 100 kg/m <sup>2</sup> s
0.4	2.40 ± 0.06 m	59.2 ± 1.7 kg/m <sup>2</sup> s	107.1 ± 3.4 kg/m <sup>2</sup> s
0.8	2.08 ± 0.09 m	58.2 ± 1.6 kg/m <sup>2</sup> s	122.0 ± 3.2 kg/m <sup>2</sup> s
1.2	2.30 ± 0.08 m	56.3 ± 1.4 kg/m <sup>2</sup> s	106.6 ± 2.9 kg/m <sup>2</sup> s
1.5	1.86 ± 0.13 m	62.5 ± 1.8 kg/m <sup>2</sup> s	103.3 ± 2.7 kg/m <sup>2</sup> s
1.7	2.03 ± 0.11 m	56.4 ± 1.5 kg/m <sup>2</sup> s	98.9 ± 2.7 kg/m <sup>2</sup> s
2.1	2.08 ± 0.15 m	52.0 ± 1.3 kg/m <sup>2</sup> s	99.2 ± 2.6 kg/m <sup>2</sup> s
2.5	1.88 ± 0.24 m	69.1 ± 1.7 kg/m <sup>2</sup> s	116.8 ± 2.8 kg/m <sup>2</sup> s
Average values	2.09 ± 0.20 m	59.1 ± 5.4 kg/m <sup>2</sup> s	107.7 ± 8.7 kg/m <sup>2</sup> s

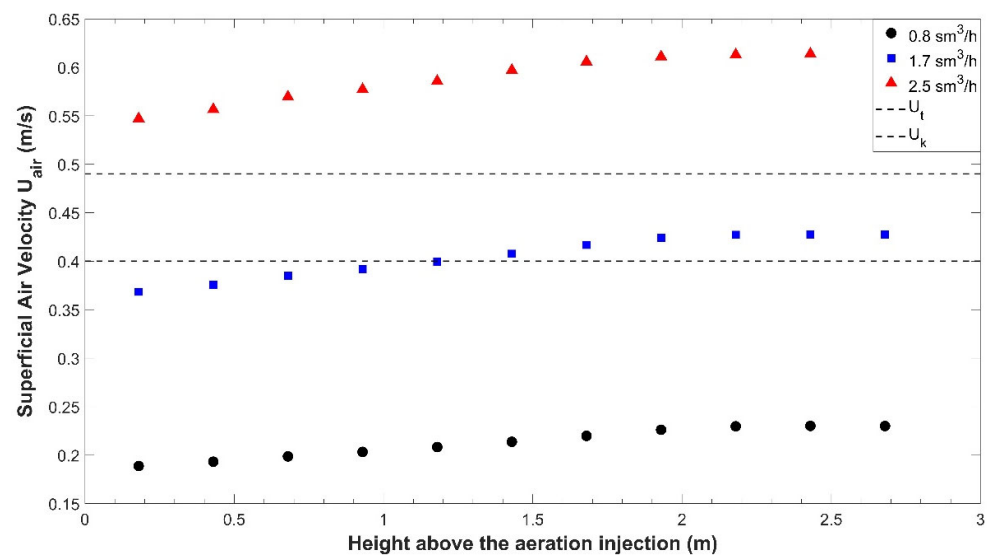


**Figure 5.** Increase of the superficial air velocity with the height in the tube, for three air flow rates, without particle circulation. The dashed lines correspond respectively to the turbulent and fast fluidization transition velocities determined with the standard fluidization column.

#### 4.2. Identification of the Fluidization Regimes in the Tube

The recorded pressure signals have been analysed by the methods presented in Section 3 to identify the fluidization regimes in each configuration.

##### 4.2.1. Solid Volume Fraction

The shape of the evolution of the solid volume fraction  $\alpha_i$  with the tube height can be an indicator of the fluidization regime. Figure 6 shows three evolutions for the same tests as presented in the previous section. The corresponding air velocities at the level of the aeration injection are indicated in the titles of the sub-figures. The bars are representative of the pressure fluctuations. In Figure 6a, the superficial air velocity is lower than  $U_t$  (cf. Figure 5) confirming, with the visual observations, that the suspension is in the slugging regime. Here,  $\alpha_i$  slightly decreases with the height of the bed due to the coalescence of the bubbles, and the surface of the suspension is measured at approximately 2 m. The sensors above this limit measure nearly zero because there is no particle. Then, in Figure 6c, the superficial air velocity is higher than  $U_k$  and the evolution of  $\alpha_i$  is clearly different. There is a dense zone where  $\alpha_i$  decreases with the bed height, followed by a dilute zone where the measured pressure drop is not zero. The shape of this evolution is clearly a characteristic of the fast fluidization regime as explained in [20]. Furthermore, in this regime, clusters of particles are entrained upward, which was visually confirmed. Based on the air velocities, the test in Figure 6b should correspond to an intermediate between the slugging and the fast fluidization regime. A dilute zone exists, which is less marked than the one in Figure 6c. However, there is no cluster visually observed, which confirms that the test is not in the fast fluidization regime. This test could be representative of a turbulent regime. This is discussed in the following sections.

Tests with particle circulation are not presented but the evolutions of  $\alpha_i$  show similar shapes for aeration air flow rates of 0.8 and 2.5 sm<sup>3</sup>/h, thus representative of the slugging and fast fluidization regimes respectively. However, for 1.7 sm<sup>3</sup>/h aeration, the evolution with particle circulation is similar to the one in Figure 6a, i.e., representative of the slugging regime. This trend is explained by the variation of the slip velocity  $U_{slip} = U_{air} - U_p$ , i.e., the difference between the upward air and particles velocities, which decreases when particles are circulating for a given air flow rate. In fact, this velocity is the pertinent parameter for defining the transitions of regime in circulating systems in simple fluidization columns according to [29].

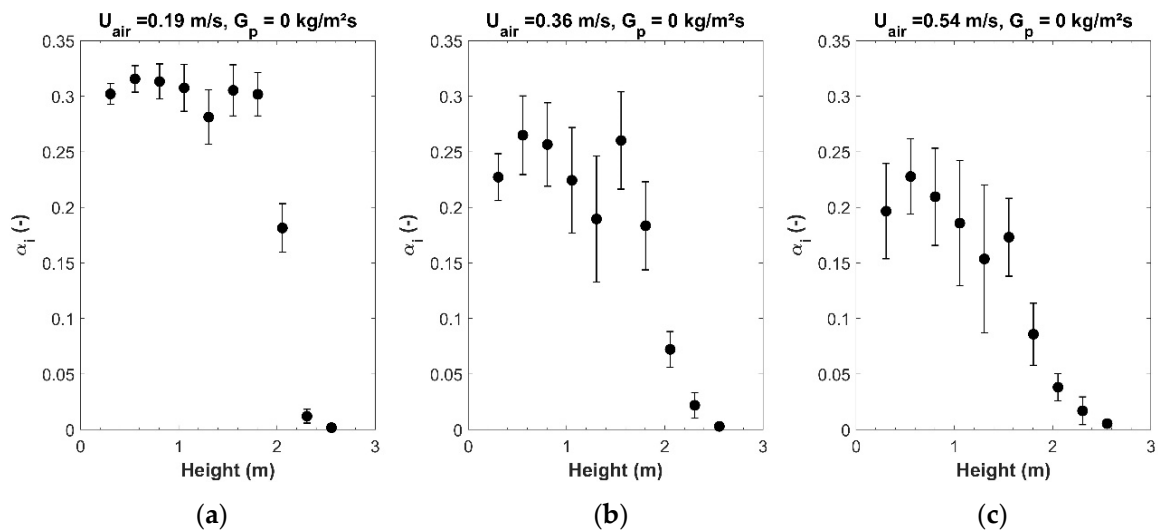


**Figure 6.** Evolution of the local solid volume fraction with the height in the tube, for three aeration flow rates: (a)  $0.8 \text{ m}^3/\text{h}$ , (b)  $1.7 \text{ m}^3/\text{h}$ , and (c)  $2.5 \text{ m}^3/\text{h}$ , without particle circulation.

It is obvious that the aeration flow rate has a strong influence on the solid volume fraction. This influence is directly presented in Figure 7 in terms of the overall solid volume fraction  $\alpha_h$ , calculated in the dense zone, versus the superficial excess air velocity in the tube  $U_{air} - U_{mf}$  at the level of the aeration injection. Three curves are presented, for the following test cases: no particle circulation, and particle mass fluxes of 50 and 100  $\text{kg/m}^2\text{s}$ . First, the increase of the aeration flow rate induces a relatively linear decrease of  $\alpha_h$  because of an increasing air volume, as was previously observed [16,17]. This means that the fluidization regime has no influence on the proportion of the volume occupied by the air. Second, it highlights a strong difference between the operation conditions: the suspension is denser with circulation than without, and  $\alpha_h$  increases with  $G_p$ . This is because the particle circulation induces a stronger pressure drop, especially due to the acceleration term (see Section 3.1).

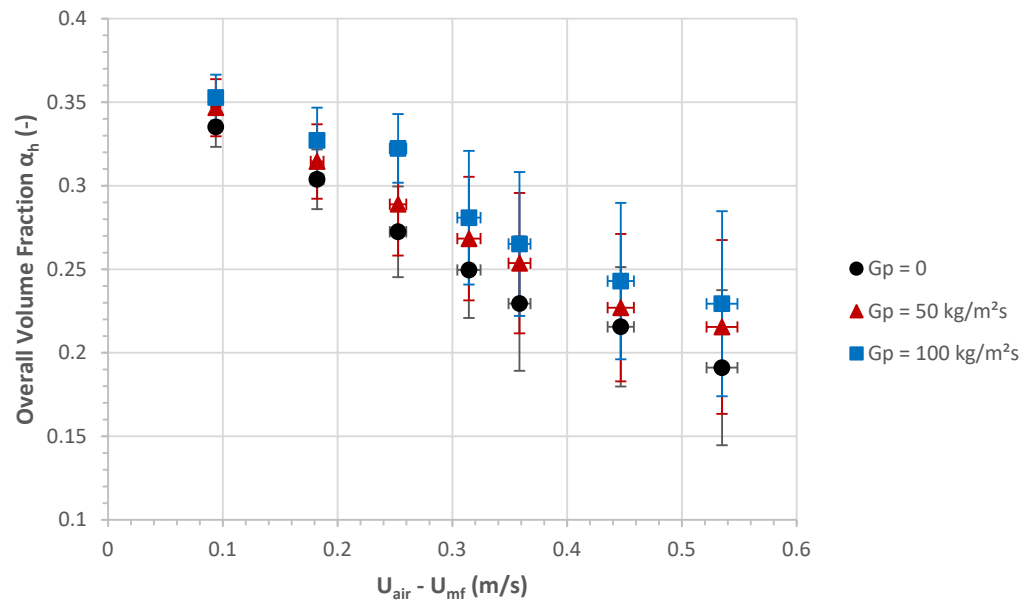


**Figure 7.** Evolution of the overall solid volume fraction versus the superficial excess air velocity in tube, for three particles mass fluxes.

#### 4.2.2. Power Spectrum Analyses

The spectra obtained with the coherence analysis detailed in Section 3.2 are analysed and compared with the data presented in the previous section to identify the fluidization regimes in the tube. One starts with the analysis of spectra obtained with the  $P_{tot}$  signal pressure, i.e., in the dispenser (Figure 8). As this signal is the chosen reference of the coherence analysis, the spectra are simple PSD's. The frequency axis is limited to 5 Hz because the higher ones are not relevant in this study. The spectra show three different flow configurations. Figure 8a presents the configuration defined by  $0.4 \text{ sm}^3/\text{h}$  of aeration flow rate and no particles circulation. The exploding bubbling regime in the dispenser is easily identifiable by a peak at 1.8 Hz, with a very low magnitude characteristic of bubble induced pressure fluctuations. There are also several peaks above 0.2 Hz, which could be representative of the slight transient regime, always present, and of the oscillations at the bed surface. Figure 8b corresponds to the same experimental aeration conditions as Figure 8a, but with a solid mass flux of  $59 \text{ kg/m}^2\text{s}$ . When there is circulation, the quantity of particles in the dispenser is not perfectly constant. This results in a variation of the measured  $P_{tot}$ , with a signature in the spectrum like a strong transient regime with a peak at very high magnitude around 0.1 Hz and a gradually decrease until approximately 0.2 Hz. However, a zoom on the rest of the frequencies shows a spectrum similar to the one in Figure 8a but with less information. This means that a particle flow i.e., a variation of the particle mass in the dispenser can hinder the identification of the characteristic peaks in the spectra. To reduce this phenomenon, a moving average is computed and subtracted to analyse solely the signal fluctuations. The resulting signal is then analysed by the FFT, acting like a high-pass filter. Figure 8c presents another configuration, defined by  $2.5 \text{ sm}^3/\text{h}$  of aeration flow rate and without particle circulation (i.e., the test presented in the previous sections with a fast fluidization regime in the tube). One can observe a frequency distribution below 1 Hz and associated with magnitudes much higher than those in Figure 8a. This is representative of the fast fluidization regime in the tube as identified by [36]. A small peak characteristic of the bubbling regime in the dispenser at 1.8 Hz is also detected, with a similar magnitude as the one in Figure 8a. This means that the strong pressure fluctuations caused by this regime inside the tube are recorded by  $P_{tot}$  even if there is a freely bubbling regime in the dispenser.

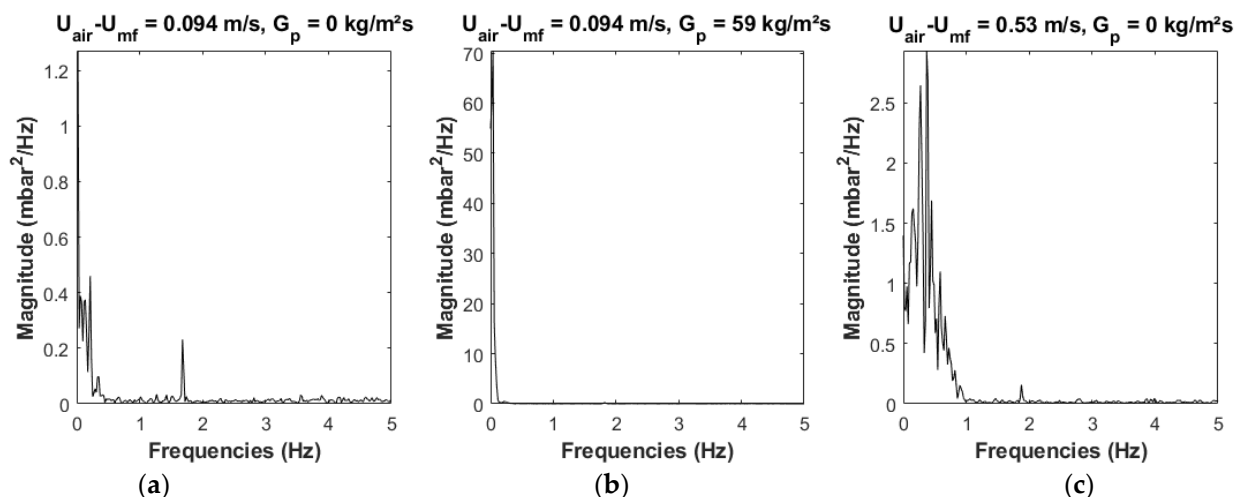


**Figure 8.** Three spectra obtained with the  $P_{tot}$  pressure signal with various experimental configurations of the air velocity and the solid mass flux, respectively (a)  $0.094 \text{ m/s}$  and  $0 \text{ kg/m}^2\text{s}$ , (b)  $0.094 \text{ m/s}$  and  $59 \text{ kg/m}^2\text{s}$ , and (c)  $0.53 \text{ m/s}$  and  $0 \text{ kg/m}^2\text{s}$ .

The coherence analysis can then be used to analyse the temporal pressure signals, for a given test, at several heights in the tube. Figure 9 shows four spectra calculated at four different heights during the same experiment with the following control parameters:

0.8 sm<sup>3</sup>/h of aeration flow rate (i.e., a superficial excess air velocity at the level of the injection of 0.18 m/s), and a particle mass flux of 58 kg/m<sup>2</sup>s. The associated heights are identified in the titles of the sub-figures. According to the air velocities and the evolution of the solid volume fraction with the height, this test should be in the slugging regime. Figure 9a indicates that the suspension is in the single bubbling regime just above the aeration, characterized by several distributions of peaks at frequencies higher than 1 Hz with small magnitudes. Along the tube height, the bubbles coalesce to form slugs [16]. At roughly 1 m above the aeration, the frequency distribution is thus shifted to lower values and the peaks are more clearly defined at 0.4–0.5 Hz and higher magnitudes (Figure 9b). There are still some higher frequencies with low magnitudes, attributed to noise. This spectrum could then be characteristic of wall slugs. Higher in the tube, the spectra are similar but this noise gradually decreases, and the characteristic peaks of slugs are associated with higher magnitudes (Figure 9c,d). This could be representative of axisymmetric slugs. In fact, the wall slugs gradually merge along the height into axisymmetric slugs [17].

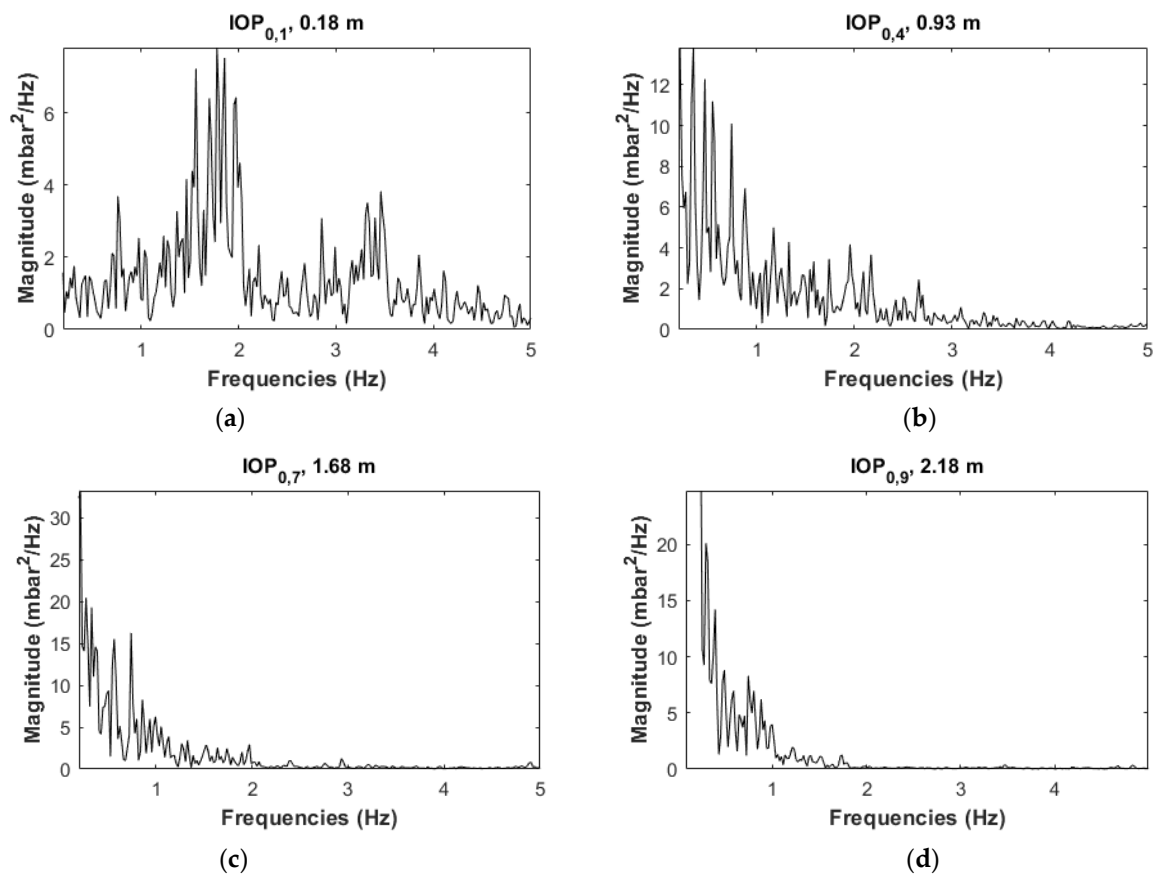


**Figure 9.** Four spectra obtained at various heights for the same experimental configuration, at  $U_{air} - U_{mf} = 0.18$  m/s and  $G_p = 58$  kg/m<sup>2</sup>s: (a) 0.18 m, (b) 0.93 m, (c) 1.68 m and (d) 2.18 m.

Two quantitative conclusions can be extracted from the power spectra given by the coherence analysis. First, it is possible to identify a dominant frequency on each spectrum, i.e., the frequency associated with the highest magnitude, representative of the main perturbation of the signal. The evolution of this quantity along the height is shown in Figure 10a, for the four spectra presented in Figure 9. A transition between the bubbling and the slugging regimes is clearly identified after the first measurement height by a strong diminution of the dominant frequency. Combining the eleven data given by the tube pressure instrumentation, this transition is identified at a height of approximately 0.7 m above the aeration, in agreement with the data from [19] in the case of a fluidization

column. It is difficult to identify a transition between the two types of slugs (wall slugs and axisymmetric slugs) along the height only from the point of view of the dominant frequencies because they remain approximately constant around 0.3 Hz. Second, the integral of each incoherent spectrum, i.e., the power of the spectrum, is proportional to the characteristic dimension of the perturbation according to [38]. The evolution of this quantity with the height is presented in Figure 10b, normalized by the maximum value obtained for this test. A strong increase of this quantity at low heights is shown, where the bubbles are coalescing to wall slugs. Then, there is a slight decrease around 2 m, which could be representative of the transition to axisymmetric slugs.

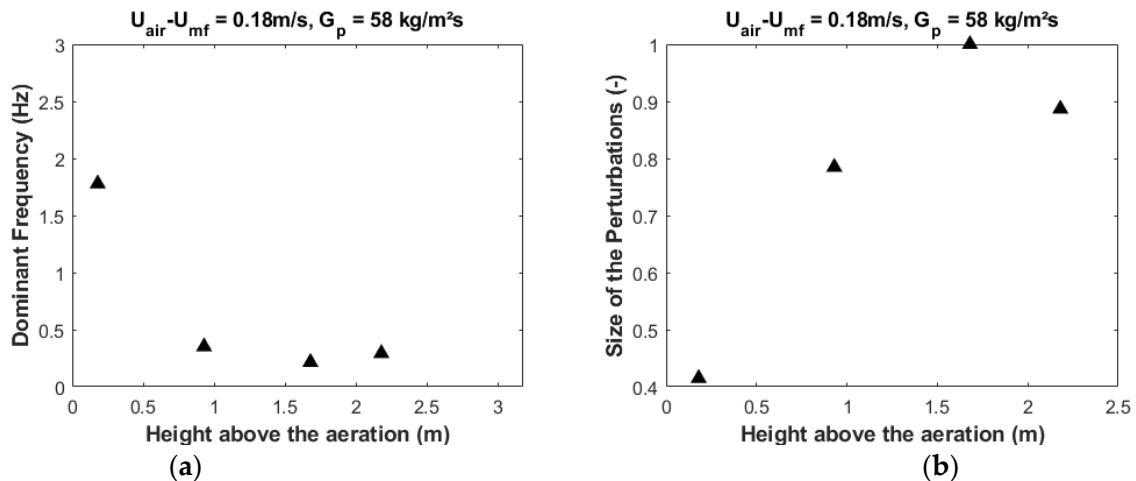


**Figure 10.** Evolutions with the height of (a) the dominant frequency of the IOP spectrum and (b) the integral of the IOP spectrum, for the same experimental configuration as for Figure 9.

Figure 11 shows a test with  $2.5 \text{ m}^3/\text{h}$  of aeration flow rate (i.e.,  $U_{air} - U_{mf}$  of  $0.53 \text{ m/s}$ ) and a particles mass flux of  $69 \text{ kg/m}^2\text{s}$  in order to compare the spectra obtained by the coherent analysis in several fluidization regimes. This test is identified as a fast fluidization regime based on the values of the air velocity higher than  $U_k$ , the decrease of the solid volume fraction with the height and the presence of a dilute zone. In the four sub-figures, which represent the spectra obtained at four different heights as previously, one notes the presence of a frequency distribution characteristic of fast fluidization [36]. The associated magnitudes are slightly varying. In fact, at  $0.18 \text{ m}$  height (Figure 11a), the aeration injector is still very close to the sensor, and the pressure fluctuations are lower than above in the tube. This results in magnitudes lower too, even if they remain much higher than in the bubbling and slugging regimes. Moreover, at  $2.18 \text{ m}$  (Figure 11d), the suspension is diluted, as confirmed by the evolution of  $\alpha_i$  with height (cf. Figure 6). The magnitudes are slightly lower in the tube but the frequency distribution is still present, which corresponds to the fast fluidization regime.

As previously, the four spectra presented in Figure 11 are used to extract both their dominant frequencies and their integrals. These values are presented in Figure 12. In Figure 12a, no evolution of the dominant frequency with the height is evidenced. This differs from the previous plot related to a slugging regime case. The mean value is approximately  $0.3 \text{ Hz}$  even in the dilute zone. Furthermore, one can observe in Figure 12b that the size of the perturbations increases with the height, with a very slight decrease in the dilute zone. These two results confirm that there is no transition of the flow regime along the tube height.



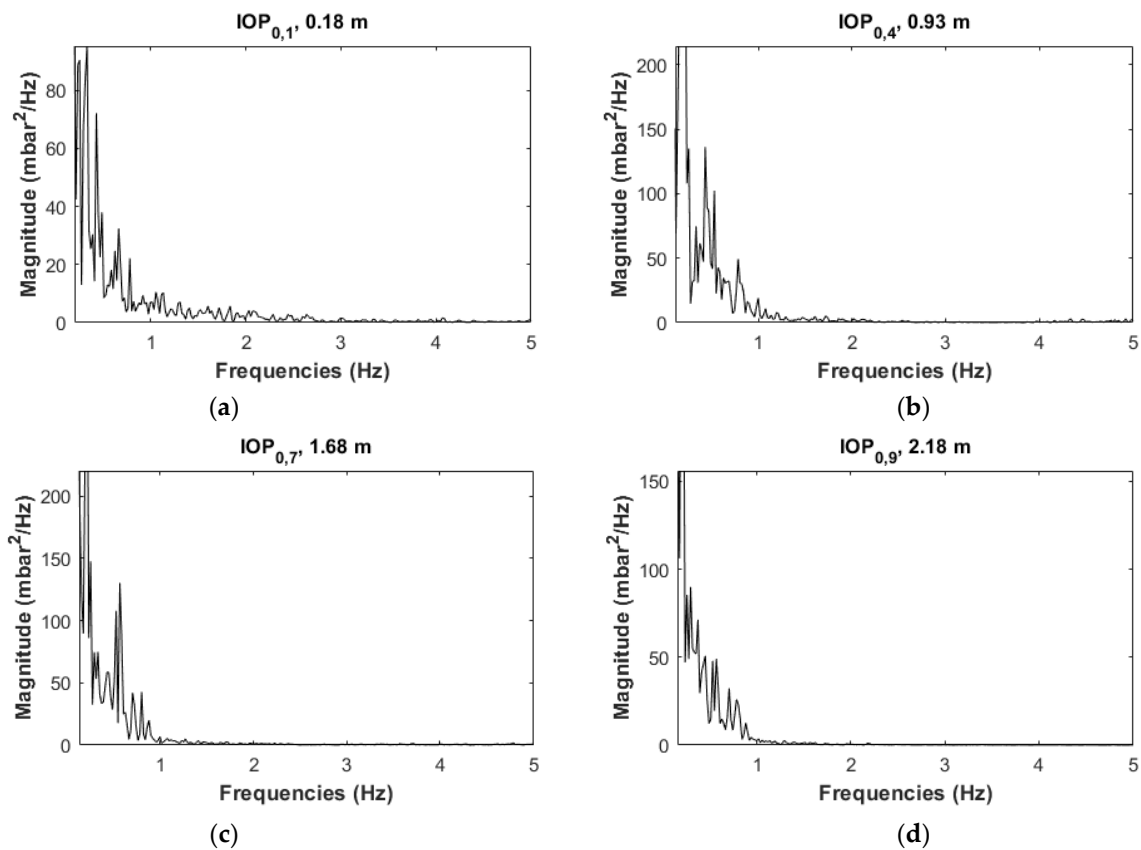


**Figure 11.** Four spectra obtained at various heights for the same experimental configuration, at  $U_{\text{air}} - U_{\text{mf}} = 0.53 \text{ m/s}$  and  $G_p = 69 \text{ kg/m}^2\text{s}$ : (a) 0.18 m, (b) 0.93 m, (c) 1.68 m and (d) 2.18 m.

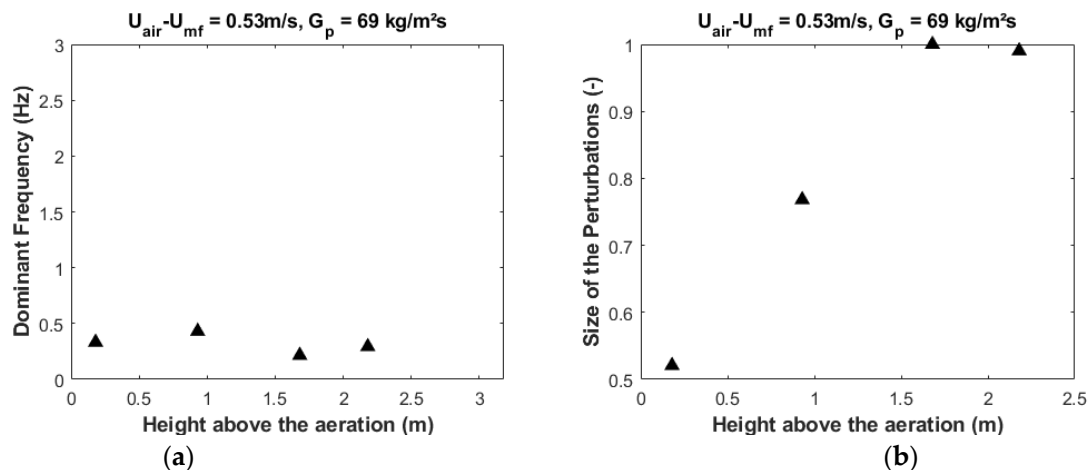


**Figure 12.** Evolutions with the height of (a) the dominant frequency of the IOP spectrum and (b) the integral of the IOP spectrum, for the same experimental configuration as for Figure 11.

The coherence analysis confirms the presence of a slugging and a fast fluidization regime in the tube as one could expect based on the air velocity values (cf. Figure 5). The intermediate value corresponds to the turbulent regime, presented in Figure 13, with the configuration of  $1.7 \text{ m}^3/\text{h}$  aeration flow rate i.e., an air velocity at the level of the injection of  $0.36 \text{ m/s}$  and a particle mass flux of  $56 \text{ kg/m}^2\text{s}$ . As illustrated in Figure 5, the turbulent velocity  $U_t$  is reached due to the depressurization that results in the increase of the air velocity with the height. In Figure 13a, a frequency distribution similar to the fast fluidization regime is identified, but the associated magnitudes are lower than in the

previous case corresponding to the single bubbling regime (cf. Figure 9a). Furthermore, one can observe noise at frequencies higher than 1 Hz and a high peak around 1.6 Hz, which is characteristic of a single bubbling regime. In Figure 13b–d, the frequency distributions are identifiable with higher magnitudes, which increase with the height and are slightly lower than the ones in the fast fluidization regime. Such evolution could be characteristic of the turbulent regime. As previously observed, strong pressure fluctuations caused by the fast fluidization regime in the tube are recorded in the dispenser (cf. Figure 8). Thus, it appears that the pressure fluctuations induced by the turbulent regime in the upper part of the tube have a signature in the bottom part of the tube and the dispenser even if the suspension experiences a single bubbling regime in this zone.

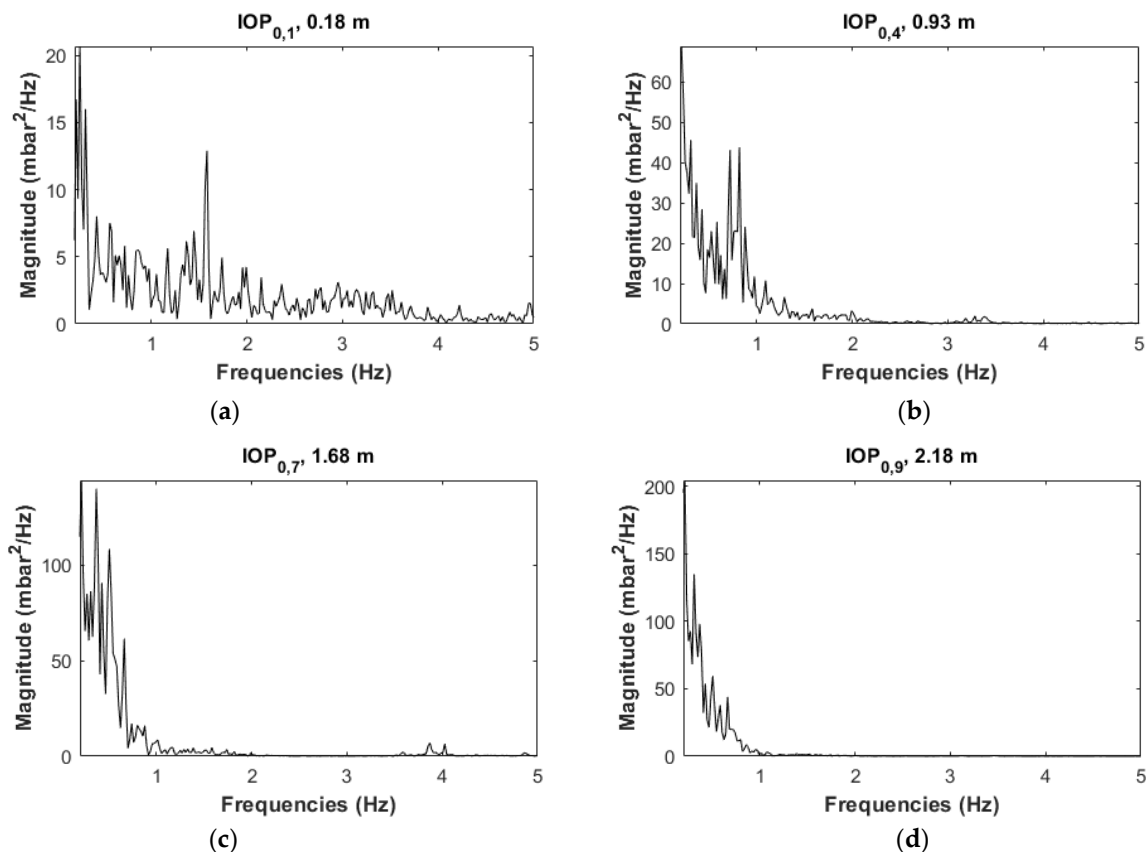


**Figure 13.** Four spectra obtained at various heights for the same experimental configuration, at  $U_{air} - U_{mf} = 0.36$  m/s and  $G_p = 56$  kg/m<sup>2</sup>s: (a) 0.18 m, (b) 0.93 m, (c) 1.68 m and (d) 2.18 m.

The extracted dominant frequencies of the four spectra presented in Figure 13 are relatively constant with the height, around 0.25 Hz, even in the bubbling regime at the level of the first sensor (Figure 14a). This is due to the higher magnitudes of the frequency distribution recorded at 0.18 m associated with the turbulent regime. Contrary to the fast fluidization regime, the size of the perturbations increases with the height in the tube, without any decrease in the upper part (Figure 14b). This means that there is no dilute zone for this test. In conclusion, the difference between the turbulent and the fast fluidization regimes is small and difficult to identify from solely a frequency point of view. Both of the regimes show a frequency distribution on their power spectra. However, integrating the different methods of analyses, the fast fluidization is characterized by the presence of a dilute zone even with particle circulation. This zone can be clearly identified by both the evolution of  $\alpha_i$  with the height and the smaller magnitudes of the characteristic peaks in the associated spectra (which is also associated with a decrease of the perturbation size). These phenomena are not present in the turbulent regime. Furthermore, the turbulent

regime is characterized by the presence of a single bubbling regime at the bottom of the tube, while the fast fluidization regime shows no regime transition with the height.

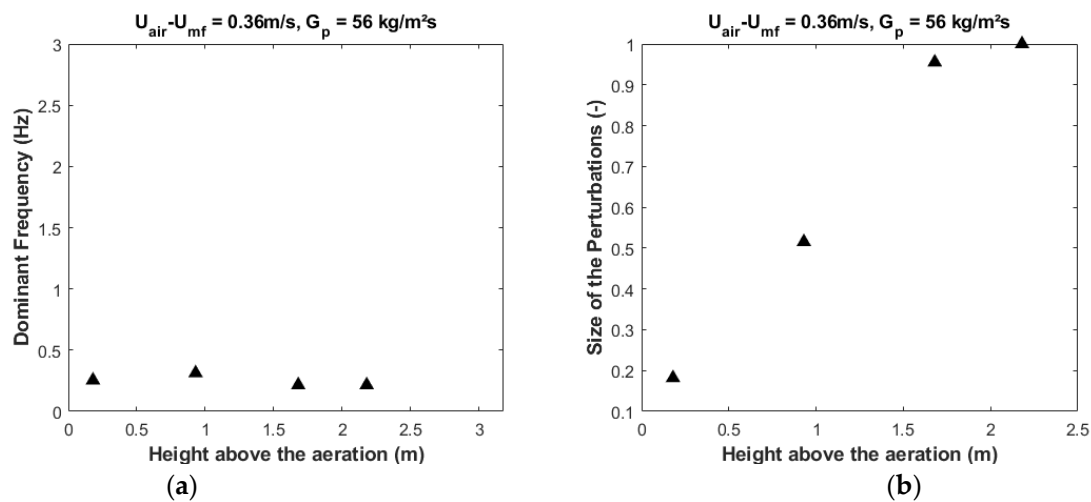


**Figure 14.** Evolutions with the height of (a) the dominant frequency of the IOP spectrum and (b) the integral of the IOP spectrum, for the same experimental configuration as for Figure 13.

In conclusion, the coherence analysis is a useful tool for fluidization regime identification based on the shape of the spectra but also on the frequencies and magnitudes of the dominant peaks. The evolution of the dominant frequency with height enables the clear identification of a transition from bubbling to slugging. However, this frequency does not vary with the control parameters and remains in the range of 0.2–0.4 Hz. This value is in accordance with the observations of [19] in the case of a fluidization column, and of [16,17] for a similar system. For the turbulent and the fast fluidization regimes, a frequency distribution is observed, then the dominant frequency does not have a real meaning. The evolution of the perturbation size is discussed in Section 4.2.4.

#### 4.2.3. Cross-Correlation Analyses

Another method allows analysis of temporal pressure signals, namely cross-correlation. Figure 15 shows four evolutions of the cross-correlation function, corresponding to the four regimes identified in the previous sections. This method is not sufficiently accurate to detect the velocity of the perturbations that produce small pressure fluctuations, as shown in Figure 15a for the single bubbling regime (at the bottom of the tube, for a test with  $0.8 \text{ m}^3/\text{h}$  of aeration flow rate). It corresponds to the small peaks not crossing the average value of the pressure signal. Figure 15b is related to the same test as Figure 15a, but for a pressure sensor located 1.68 m above the aeration, i.e., in the wall-slugging regime. As explained before, the wall slugs progressively merge into axisymmetric slugs, detected approximately at this height. This explains why the evolution of the function is not perfectly smooth but has a stepped shape, which corresponds to the “noisy” peaks after 1 Hz in the power spectra (cf. Figure 9). The identified maximum corresponds to an upward velocity of the slug of  $U_s = 0.42 \pm 0.04 \text{ m/s}$ . Figure 15c,d correspond to tests at 1.7 and  $2.5 \text{ m}^3/\text{h}$  aeration flow rates respectively, i.e., leading to a turbulent and a fast fluidization regimes. Since there is no noise on the associated power spectra, the cross-correlation functions exhibit smoothed shapes. The upward velocities of the perturbations are higher than in the slugging configuration, of  $0.83 \pm 0.14$  and  $1 \pm 0.20 \text{ m/s}$  respectively. In the fast fluidization case, a phase inversion occurs, and the velocity measured by the cross-correlation is then relative to clusters of particles [20].

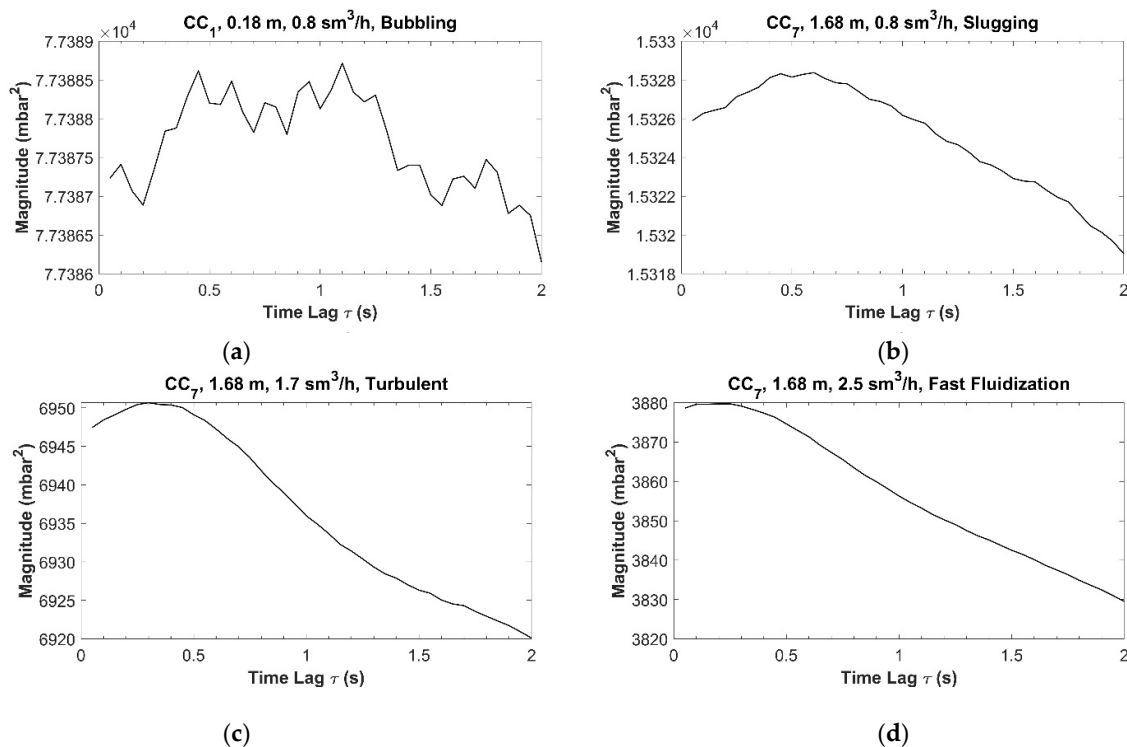


**Figure 15.** Several cross-correlation functions corresponding to different fluidization regimes in the tube, at various heights and aeration flow rates: (a) single bubbling, (b) wall-slugging, (c) turbulent, and (d) fast fluidization.

The previous results indicate that varying the aeration flow rate induces variations of the upward velocity of voids and clusters detected by the cross-correlation method. Combining all the tests, it seems that the increase of the particles mass flux leads also to an increase of the measured upward velocity. This tendency is represented in Figure 16. As the cross-correlation cannot detect bubbles and their velocities, the 1.68 m height has been fixed to compare the velocities measured in slugging, turbulent and fast fluidization regimes with the theory. In the Figure, values are plotted versus the sum of the excess air velocity and the upward particles velocity,  $U_p = G_p / \rho_p \alpha_i$ , for the various  $G_p$  values. The dashed line in the Figure represents the upward slugs velocities calculated with the two-phase theory of fluidization for the case of axisymmetric slugs, where  $U_{s,th} = U_{air} - U_{mf} + U_p + k\sqrt{gD_t}$  (in a fluidization column) [33,39]. In this equation, a coefficient  $k$  of 0.35 or 0.7 applies for the axisymmetric or the wall slugging regime respectively. The theoretical velocities for wall slugs are not presented in the Figure for the sake of clarity, because the two theoretical curves are very similar. For the tests leading to a slugging regime, i.e., for low aeration flow rates, the measured velocities are in good agreement with the two-phase theory. However, for the turbulent and fast fluidization regimes, the measured velocities are higher than 1 m/s i.e., higher than the value estimated with the theory for the slugging regime which confirms the regime transition. However, uncertainties are strong (approximately 20% and more of relative error). Consequently, this method has a limited accuracy for high perturbation velocities, due to the low acquisition frequency imposed (20 Hz). In conclusion, the use of the cross-correlation function gives upward void velocities in good agreement with the two-phase theory for the slugging regimes, at low air velocities. At higher air velocities, the method is not accurate but allows the identification of high upward velocities of voids and particles (clusters) for the turbulent and fast fluidization regimes, respectively.

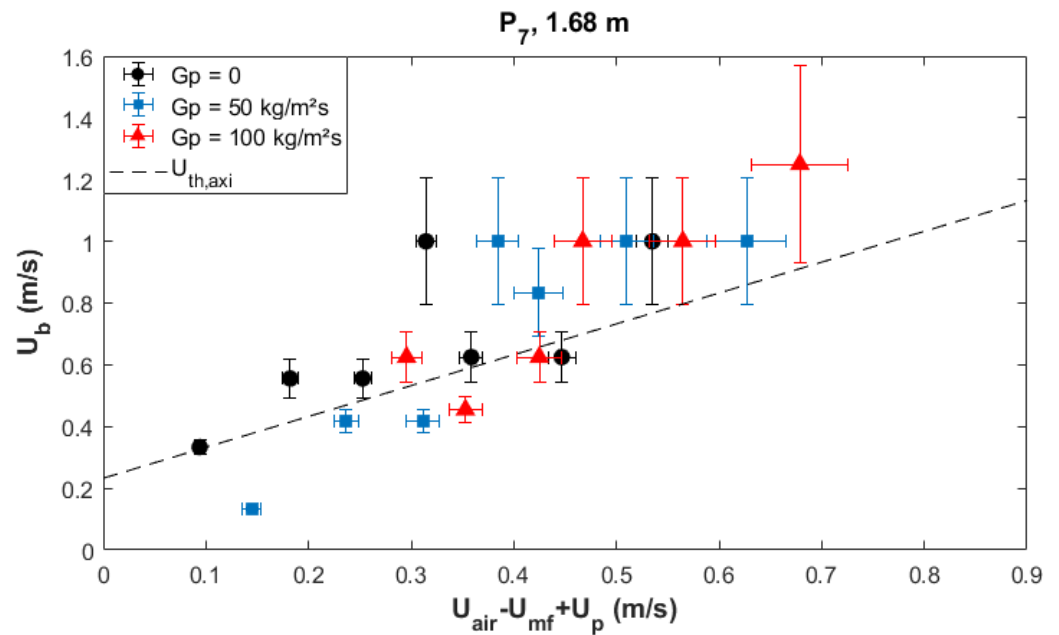


**Figure 16.** Evolution of the upward velocity measured with the cross-correlation function at 1.68 m above the aeration versus  $U_{air} - U_{mf} + U_p$ , with the particles mass flux as a parameter. The dashed line represents the velocities calculated by the two-phase theory for the case of axisymmetric slugs.

#### 4.2.4. Pressure Fluctuations Amplitude

Finally, the last method consists of a direct study of the relative pressure fluctuations in the tube. This quantity is defined as the ratio between the standard deviation of a differential temporal pressure signal and its mean value,  $\sigma(\Delta P_i) / \overline{\Delta P_i}$ . Figure 17 illustrates representative results of all the tests carried out. The plots evidence three main trends. First, the transitions of regimes appear more clearly in the non-particle circulation mode than in the particle circulation mode. Second, pressure fluctuations are more intense in the former mode than in the latter mode. Third, the pressure fluctuations increase with the height in the tube for a given fluidization regime.

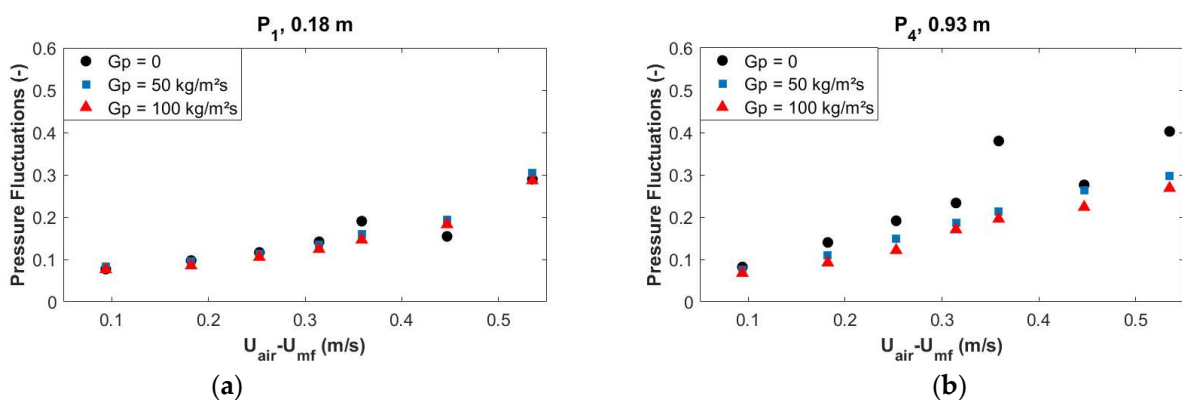


**Figure 17.** Cont.

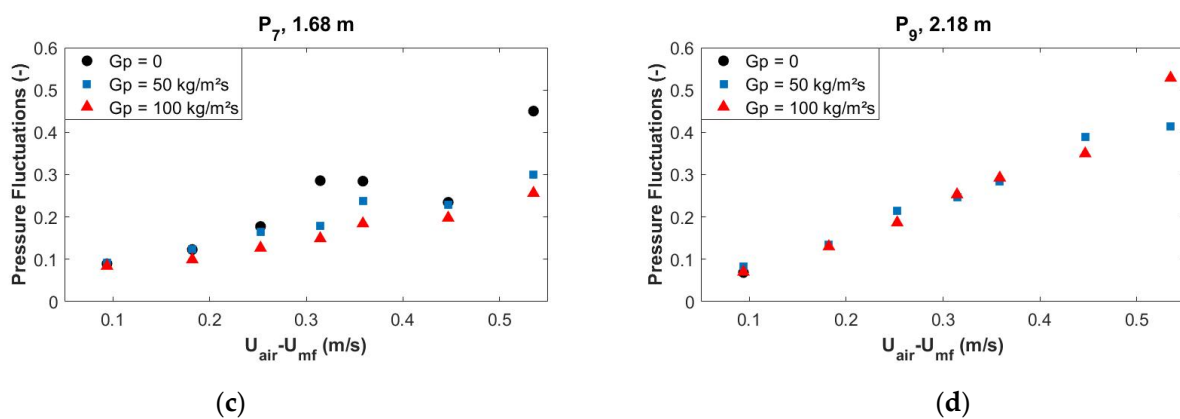


**Figure 17.** Evolutions of the pressure fluctuations with superficial excess air velocity (calculated at the level of the aeration), for three particle mass flux configurations, at fixed heights: (a) 0.18 m, (b) 0.93 m, (c) 1.68 m and (d) 2.18 m.

The regime transitions can be associated with amplitude levels of the pressure fluctuations. According to [19], the slugging regime occurs in a fluidization column when the relative pressure fluctuations reach 10%. In fact, in Figure 17, the relative pressure fluctuations associated with low air velocities i.e., points in slugging regime are approximately 10–15%, with an increase in height because of the slug coalescence. Then, by grouping the results of the sub-figures, one notes that the turbulent regime corresponds to relative fluctuations of around 15–20%, and the fast fluidization corresponds to relative fluctuations higher than 20%, also with an increase with the height in the tube.

The pressure fluctuations slightly decrease when the particles are circulating. This is due to the decrease of the relative velocity of air with respect to particles expressed by the slip velocity  $U_{slip}$  as for the solid volume fraction presented in Section 4.2.1. Then, for a given height, the amplitude of the pressure fluctuation increases with the aeration flow rate. On Figure 17a–c, one notes the transition to the turbulent regime when the pressure fluctuations reach an upper peak, in the same way as for the identification of the turbulent velocity  $U_k$  with the fluidization column (see Section 2.2). The transition is much marked without particle circulation because the circulation causes a diminution of the quantity of particles in the dispenser, which hinders the identification of the phenomena as explained in the previous sections. The value of the air velocity corresponding to the turbulent transition is of the order of the  $U_t$  velocity determined previously.

For a given regime, the amplitudes of the pressure fluctuations are increasing with the tube height. However, the increase rate may vary depending on the regime. This phenomenon is mainly due to void coalescence. In fact, the evolutions of the pressure fluctuations are strongly correlated with the evolutions of the perturbation size presented in Section 4.2.2. This confirms the Parseval's identity, where the power of a signal is kept regardless the representation:  $\int |P_i(t)|^2 dt = \int |E_i(f)|^2 df$  [40]. It also means that the power spectra obtained by the coherence analysis are consistent.

#### 4.3. Synthesis

A combination of analysis methods of pressure signal is necessary to identify and characterize the various fluidization regimes encountered in the particle-in-tube concept. The incoherent analysis (in the frequency domain), the cross-correlation (in the temporal domain), and the amplitude of differential pressure fluctuations are used as complementary approaches, following the same methodology as for the risers [34–38]. Two main gas-solid flow behaviours are identified as a function of tube height and air velocity, (1) coexistence of two fluidization regimes inside the tube and (2) single fluidization regime. In the former state, two cases happen: bubbling and slugging regimes, and bubbling and turbulent regimes. Fast fluidization corresponds to the latter state.



In the bubbling-slugging state, the transition from bubbles to wall slugs is always observed approximately 0.7 m above the aeration injection, as observed by [17,19]. This transition is evidenced by a strong diminution of the dominant frequency with height. On the power spectra, there is a shift of the frequency distribution to low values, with a dominant peak around 0.2–0.4 Hz and increasing magnitudes. Wall slugs can be seen as an unestablished slugging regime, which explains the presence of peaks with low magnitudes after 1 Hz. These wall slugs are progressively transforming into axisymmetric slugs. The power spectra are similar, but there is no more noise after 1 Hz at a height of approximately 1.7 m. Furthermore, the cross-correlation functions are smoothed while for wall slugs they are stepped shapes and allow the identification of upward slug velocities around 0.4 m/s. These values are in good agreement with the prediction of the two-phase theory of fluidization [33,39].

In the bubbling-turbulent state, the air velocity ranges between the turbulent and the fast fluidization velocities,  $U_t$  and  $U_k$ . The single bubbling regime is still present at the bottom of the tube, with the same characteristics as for the previous situation. Moreover, one can observe a distribution of frequencies below 1 Hz on the power spectra. Although representative of the turbulent regime, this distribution is associated with magnitudes too low for an established turbulent regime. Nevertheless, it highlights the presence of a turbulent regime higher in the tube. This transition from the bubbling to the turbulent regime is observed around 0.7 m above the aeration. The cross-correlation functions are smooth and allow the detection of upward velocities higher than one meter per second. This is higher than the velocities predicted by the slug's theory, which does not apply anymore.

In the fast fluidization state, the air velocity is higher than the fast fluidization velocity  $U_k$ . The fast fluidization regime is identified along the entire tube height. It can be identified in the power spectra by a distribution of frequencies above 1 Hz associated with high magnitudes (higher than for the turbulent regime). These magnitudes increase with the height while the frequencies remain constant. The dominant frequency remains constant with the height and equal roughly 0.3 Hz. The cross-correlation functions are smooth and the highest upward velocities among all the regimes are determined. However, because of the data acquisition frequency, the accuracy of the detected velocity is quite low. The suspension shows a relatively dense part followed by a dilute part easily distinguishable on the evolution of the particles volume fraction with the height.

Moreover, let us estimate the power consumption induced by the air injections in an industrial scale solar receiver. In the particle-in-tube concept, the turbulent fluidization regime is reached with an aeration flow rate of around  $1.7 \text{ m}^3/\text{h}$  according to the previous results. At industrial scale, a  $50 \text{ MW}_{\text{th}}$  solar receiver is feasible with 360 tubes based on preliminary calculations, and an overall electrical power of approximately 15 MW [6,7]. The geometry of the receiver and the dispenser were simulated, and an air flow rate of  $2700 \text{ m}^3/\text{h}$  was calculated to obtain the same fluidization velocity in the dispenser as in this paper. The total air consumption that corresponds to the turbulent fluidization regime in the receiver tubes is thus around  $3300 \text{ m}^3/\text{h}$ . Considering a typical modern industrial compressor that can supply pressurized air at 7 bars with a consumption of  $0.108 \text{ kW}/(\text{m}^3 \cdot \text{h})$ , this corresponds to a power consumption of approximately 360 kW, i.e., approximately 2.4% of the solar plant nominal power.

## 5. Conclusions

The different fluidization regimes are studied in an upward gas-particle dense suspension flowing in a tube with large aspect ratio at ambient temperature, which greatly differs from commonly used risers. Group A olivine particles ( $d_{sv} = 61 \mu\text{m}$ ) are used and air velocity varies in the range 0.1–0.65 m/s. The regimes encountered in the tube are identified thanks to various temporal pressure signal processing methods, applied in the case of risers, the combination of which results in improved sensitivity of the identification process while allowing a short acquisition time.

Along the tube height, bubbling-slugging, bubbling-turbulent and fast fluidization regime configurations are observed as a function of air velocity.

From the solar receiver operation viewpoint, two main conclusions can be derived from the experimental results. They address the comparison between without and with particle circulation flow behaviour and recommendation for on-sun operations.

First, the suspension is denser along the tube height with particle circulation than without. For air velocity varying in the range 0.1–0.53 m/s, the mean particle volume fraction decreases from 0.34 to 0.19 and from 0.35 to 0.23 without and with particle circulation respectively. Indeed, the ignition of a particle flow rate induces a supplementary pressure drop term in the pressure balance that leads to a decrease of the bed porosity. For a given air flow rate, the circulation ignition might induce a change of fluidization regime. Furthermore, the transitions between the fluidization regimes are more easily identifiable without particle circulation, in particular because of the transient mode induced by the particle flow. Moreover, the particle circulation shows no impact on the measured upward voids velocities.

Second, based on this work and previous studies [17,19], the turbulent regime would be the most favourable regime for on-sun operation in order to maximize the wall-to-bed heat transfer and thus the receiver efficiency. Nevertheless, the particle temperature can affect the behaviour of the fluidized suspension. In fact, an increase of the temperature leads both to a decrease of the minimum fluidization velocity  $U_{mf}$  and to an extension of the bubbling domain. Thus, the transitions between the fluidization regimes will be significantly modified with the operation temperature.

Work in progress will address the examination of the temperature effect on fluidization regimes and associated heat transfer using a single tube solar receiver.

**Author Contributions:** Conceptualization, supervision, and resources, G.F.; methodology, software and investigation, R.G.; validation and formal analysis, S.M., A.T., F.B. and G.F.; data curation, G.S.; writing—original draft preparation, R.G. and G.S.; writing—review and editing, S.M., A.T., F.B. and G.F.; funding acquisition, G.F. All authors have read and agreed to the published version of the manuscript.

**Funding:** This work was funded by the French “Investments for the future” (“*Investissements d’Avenir*”) programme managed by the National Agency for Research (ANR) under contract ANR-10-LABX-22-01 (labex SOLSTICE). Additional funding was awarded by the European Union’s Horizon 2020 research and innovation program under Grant Agreement 727762, Next-CSP project. Additional funding was obtained by the Occitanie French region for the cold mock-up installation.

**Institutional Review Board Statement:** Not applicable.

**Informed Consent Statement:** Not applicable.

**Data Availability Statement:** The data presented in this study are available on request from the corresponding author.

**Acknowledgments:** The characterization of the olivine sample was conducted with the help of the Material Characterization Platform—Surfaces and Interfaces Analyses of the PROMES (CNRS) laboratory.

**Conflicts of Interest:** The authors declare no conflict of interest.

## Nomenclature

$Ar$	Archimedes number (-)
$C_D$	Friction coefficient (-)
$d_{SV}$	Sauter diameter of the olivine sample ( $\mu\text{m}$ )
$d_V$	Volume diameter of the olivine sample ( $\mu\text{m}$ )
$d_X$	Diameter corresponding to the X% value on the cumulated particle size distribution
$D_t$	Internal diameter of the glass tube (m)

$f_{acq}$	Acquisition frequency (Hz)
$F_i$	Fourier transform of the $P_i(t)$ signal
$g$	Standard acceleration due to gravity ( $m/s^2$ )
$\dot{G}_p$	Particle mass flux ( $kg/m^2s$ )
$H_{bed}$	Height of the suspension inside the tube (m)
$H_t$	Height of the glass tube (m)
$IO P_{0i}$	Incoherent part of the $i^{th}$ pressure signal
$\dot{m}_p$	Particle mass flow rate ( $kg/h$ )
$M$	Number of groups of $N$ points each used in the PSD calculation
$N_{acq}$	Number of points recorded in an acquisition
$P_{tot}$	Total relative pressure of the dispenser (mbar)
$P_i$	Relative pressure in the tube at the level of a pressure probe (mbar)
$\dot{q}_{ae}$	Aeration air flow rate in the tube ( $sm^3/h$ )
$\dot{q}_f$	Fluidization air flow rate through the dispenser ( $sm^3/h$ )
$R_{i,i+1}$	Cross-correlation function between the $P_i$ and $P_{i+1}$ pressure signals
$S_{disp}$	Section of the dispenser ( $m^2$ )
$S_t$	Section of the tube ( $m^2$ )
$U_{ae}$	Superficial aeration air velocity in the tube, due to $\dot{q}_{ae}$ (m/s)
$U_{air}$	Superficial total air velocity in the tube, $U_{ae} + U_f$ (m/s)
$U_f$	Superficial air velocity in the dispenser, due to $\dot{q}_f$ (m/s)
$U_s$	Upward slug velocity (m/s)
$U_{s,th}$	Upward slug velocity, calculated with the two-phases theory (m/s)
$U_{slip}$	Slip velocity between the air and the particles (m/s)
$U_v$	Upward void velocity, determined by the cross-correlation method (m/s)
$U_{mb}$	Minimum bubbling velocity (m/s)
$U_{mf}$	Minimum fluidization velocity (m/s)
$U_k$	Fast fluidization velocity (m/s)
$U_p$	Upward particle velocity (m/s)
$U_t$	Turbulent velocity (m/s)
$\alpha_i$	Local solid volume fraction in the tube, measured between two pressure sockets (-)
$\alpha_h$	Overall solid volume fraction in the tube (-)
$\alpha_p$	Particle volume fraction (-)
$\gamma_{0i}^2$	Coherence between the $i^{th}$ pressure signal and the "0" reference (-)
$\Delta h$	Distance between two sockets in the tube (m)
$\Delta P_{acc}$	Pressure drop due to the acceleration of the particles (mbar)
$\Delta P_{fr}$	Pressure drop due to the friction against the tube walls (mbar)
$\Delta P_i$	Differential pressure in the tube between two pressure sockets (mbar)
$\Delta P_p$	Pressure drop due to the effective weight of the suspension (mbar)
$\varepsilon$	Porosity (-)
$\rho_{air}$	Density of the air ( $kg/m^3$ )
$\rho_p$	Bulk density of the olivine ( $kg/m^3$ )
$\sigma$	Spread of the olivine sample (-)
$\sigma(P_i)$	Standard deviation of the $P_i$ pressure signal (mbar)
$\varphi$	Mean sphericity of the olivine sample (-)
$\phi_{0i}$	Cross Power Spectral Density between the $i^{th}$ pressure signal and the "0" reference
$\phi_{ii}$	Power Spectral Density of the $i^{th}$ pressure signal
$\tau$	Time lag of the cross-correlation function (s)

## Appendix A. Instrumentation of the Mock-Up

Table A1 below presents the characteristics of the instrumentation used in this paper. Two kind of pressure sensors have been used because of their respective accuracies and response times. The differential sensors are very accurate in terms of pressure measurements, but too slow to be used with dynamic treatments. It is the contrary for the relative pressure sensors. They are connected to data acquisition systems related to their response times.

**Table A1.** Instrumentation of the experimental rig.

Device	Brand	Model	Measurement Range	$f_{acq,max}$ (Hz) or $\tau_{99}$ (s)	Use
Relative Pressure Sensors	Keller	PR33X	0–500 mbar	8 Hz	$P_{tot}$ P1–P11
	Siemens	7MF1641	0–600 mbar	5 ms	
Differential Pressure Sensors	Rosemont	2051C	0–50 mbar	0.6 Hz	$\Delta P1-\Delta P10$ and $\Delta P_{disp}$
Flowmeters	Brooks	5853E	0–2.5 sm <sup>3</sup> /h	∅	$\dot{q}_{ae}$
	Brooks	5853S	0–16.8 sm <sup>3</sup> /h	∅	$\dot{q}_f$
Acquisition Systems	GraphTec	Midi Logger GL840	20 Inputs	1 Hz	Acquisition of the $\Delta P_i$
	National Instruments	USB-6218	16 Inputs	15,625 kHz	Acquisition of the $P_i$

## References

- Benoit, H.; Spreafico, L.; Gauthier, D.; Flamant, G. Review of heat transfer fluids in tube-receivers used in concentrating solar thermal systems: Properties and heat transfer coefficients. *Renew. Sustain. Energy Rev.* **2016**, *55*, 298–315. [\[CrossRef\]](#)
- Zhang, H.; Kong, W.; Tan, T.; Baeyens, J. High-efficiency concentrated solar power plants need appropriate materials for high-temperature heat capture, conveying and storage. *Energy* **2017**, *139*, 52–64. [\[CrossRef\]](#)
- Ho, C.K.; Christian, J.; Yellowhair, J.; Jeter, S.; Golob, M.; Nguyen, C.; Repole, K.; Abdel-Khalik, S.; Siegel, N.; Al-Ansary, H.; et al. Highlights of the high-temperature falling particle receiver project: 2012–2016. *AIP Conf. Proc.* **2017**, *1850*, 030027. [\[CrossRef\]](#)
- Wu, W.; Amsbeck, L.; Buck, R.; Uhlig, R.; Ritz-Paal, R. Proof of concept test of a centrifugal particle receiver. *Energy Procedia* **2014**, *49*, 560–568. [\[CrossRef\]](#)
- Flamant, G.; Hemati, H. Dispositif Collecteur D'énergie Solaire (Device for Collecting Solar Energy). French Patent FR 1058565, 20 October 2010. PCT Extension WO2012052661, 26 April 2012.
- Gueguen, R.; Grange, B.; Bataille, F.; Mer, S.; Flamant, G. Shaping High Efficiency, High Temperature Cavity Tubular Solar Receivers. *Energies* **2020**, *13*, 4803. [\[CrossRef\]](#)
- Behar, O.; Grange, B.; Flamant, G. Design and performance of a modular combined cycle solar power plant using the fluidized particle solar receiver technology. *Energy Convers. Manag.* **2020**, *220*, 113108. [\[CrossRef\]](#)
- Jacob, R.; Belusko, M.; Ines Fernandez, A.; Cabeza, L.F.; Saman, W.; Bruno, F. Embodied energy and cost of high temperature thermal energy storage systems for use with concentrated solar power plants. *Appl. Energy* **2016**, *180*, 586–597. [\[CrossRef\]](#)
- Kang, Q.; Flamant, G.; Dewil, R.; Baeyens, J.; Zhang, H.L.; Deng, Y.M. Particles in a circulation loop for solar energy capture and storage. *Particuology* **2019**, *43*, 149–156. [\[CrossRef\]](#)
- CSP2. Dense Suspensions of Solid Particles as a New Heat Transfer Fluid for CSP. Available online: <http://www.csp2-project.eu/> (accessed on 10 August 2021).
- Next-CSP. High Temperature Concentrated Solar Thermal Power Plant with Particle Receiver and Direct Thermal Storage. 2020. Available online: <http://next-csp.eu/> (accessed on 10 August 2021).
- Benoit, H.; Perez Lopez, I.; Gauthier, D.; Sans, J.-L.; Flamant, G. On-sun demonstration of a 750 °C heat transfer fluid for concentrating solar systems: Dense particle suspension in tube. *Sol. Energy* **2015**, *118*, 622–633. [\[CrossRef\]](#)
- Le Gal, A.; Grange, B.; Tessonnaud, M.; Perez, A.; Escape, C.; Sans, J.-L.; Flamant, G. Thermal analysis of fluidized particle flows in a finned tube solar receiver. *Sol. Energy* **2019**, *191*, 19–33. [\[CrossRef\]](#)
- Perez-Lopez, I.; Benoit, H.; Gauthier, D.; Sans, J.L.; Guillot, E.; Mazza, G.; Flamant, G. On-sun operation of a 150 kW<sub>th</sub> pilot solar receiver using dense particle suspension as heat transfer fluid. *Sol. Energy* **2016**, *137*, 463–476. [\[CrossRef\]](#)
- Boissière, B.; Ansart, R.; Gauthier, D.; Flamant, G.; Hemati, M. Experimental Hydrodynamic Study of Gas-Particle Dense Suspension Upward Flow for Application as New Heat Transfer and Storage Fluid. *Can. J. Chem. Eng.* **2015**, *93*, 317–330. [\[CrossRef\]](#)
- Sabatier, F.; Ansart, R.; Zhang, H.; Baeyens, J.; Simonin, O. Experiments support simulations by NEPTUNE CFD Code in a Upflow Bubbling Fluidized Bed reactor. *Chem. Eng. J.* **2020**, *385*, 123568. [\[CrossRef\]](#)
- Deng, Y.; Sabatier, F.; Dewil, R.; Flamant, G.; Le Gal, A.; Gueguen, R.; Baeyens, J.; Li, S.; Ansart, R. Dense upflow fluidized bed (DUFb) solar receivers of high aspect ratio: Different fluidization modes through inserting bubble rupture promoters. *Chem. Eng. J.* **2021**, *418*, 129376. [\[CrossRef\]](#)
- Geldart, D. Chap. 2: Single particles, Fixed and Quiescent Beds. In *Gas Fluidization Technology*; John Wiley & Sons Ltd.: Chichester, UK, 1986; pp. 11–32.
- Kong, W.; Tan, T.; Baeyens, J.; Flamant, G.; Zhang, H. Bubbling and slugging of Geldart group A powders in small diameters columns. *Ind. Eng. Chem. Res.* **2017**, *56*, 4136–4144. [\[CrossRef\]](#)
- Grace, J.R.; Bi, X.; Ellis, N. Chap. 9: Turbulent Fluidization. In *Essential of Fluidization Technology*; John Wiley & Sons Ltd.: Chichester, UK, 2020; pp. 163–180.
- Dodds, J.; Baluais, G. Particle size characterization. *Sci. Géologiques* **1993**, *46*, 79–104.
- Geldart, D. Types of Gas Fluidization. *Powder Technol.* **1973**, *7*, 285–292. [\[CrossRef\]](#)
- Davidson, J.F.; Harrison, D. Chap. 2: Incipient fluidization and particulate systems. In *Fluidization*; Academic Press: Cambridge, MA, USA, 1971.

24. Wu, S.Y.; Baeyens, J. Effect of operating temperature on minimum fluidization velocity. *Powder Technol.* **1991**, *67*, 217–220.
25. Kunii, D.; Levenspiel, O. Chap. 3: Fluidization and Mapping of Regimes. In *Fluidization Engineering*, 2nd ed.; Butterworth-Heinemann: Newton, MA, 1991; pp. 61–94.
26. Abrahamsen, A.R.; Geldart, D. Behaviour of Gas-Fluidized Beds of Fine Powders Part I. Homogeneous Expansion. *Powder Technol.* **1980**, *26*, 35–46. [[CrossRef](#)]
27. Grace, J.R.; Bi, X.; Ellis, N. Chap. 4: Gas Fluidization Flow Regimes. In *Essential of Fluidization Technology*; John Wiley & Sons Ltd.: Chichester, UK, 2020; pp. 55–74.
28. Bi, H.T.; Ellis, N.; Abba, I.A.; Grace, J.R. A state-of-the-art review of gas-solid turbulent fluidization. *Chem. Eng. Sci.* **2000**, *55*, 4789–4825. [[CrossRef](#)]
29. Rabinovich, E.; Kalman, H. Flow regime diagram for vertical pneumatic conveying and fluidized bed systems. *Powder Technol.* **2011**, *207*, 119–133. [[CrossRef](#)]
30. Zhang, H.; Kong, W.; Tan, T.; Flamant, G.; Baeyens, J. Experiments support an improved model for particle transport in fluidized beds. *Sci. Rep.* **2017**, *7*, 10178. [[CrossRef](#)]
31. Geldart, D. Chap. 6: Particle Entrainment and Carryover. In *Gas Fluidization Technology*; John Wiley & Sons Ltd.: Chichester, UK, 1986; pp. 123–154.
32. Srivastava, A.; Sundaresan, S. Role of wall friction in fluidization and standpipe flow. *Powder Technol.* **2002**, *124*, 45–54. [[CrossRef](#)]
33. Geldart, D. Chap. 4: Hydrodynamics of Bubbling Fluidized Beds. In *Gas Fluidization Technology*; John Wiley & Sons Ltd.: Chichester, UK, 1986; pp. 53–96.
34. Puncochar, M.; Drahos, J. Origin of pressure fluctuations in fluidized beds. *Chem. Eng. Sci.* **2005**, *60*, 1193–1197. [[CrossRef](#)]
35. Bi, H. A critical review of the complex pressure fluctuation phenomenon in gas-solids fluidized beds. *Chem. Eng. Sci.* **2007**, *62*, 3473–3493. [[CrossRef](#)]
36. Johnsson, F.; Zijerveld, R.C.; Schouten, J.C.; van den Bleek, C.M.; Leckner, B. Characterization of fluidization regimes by time-series analysis of pressure fluctuations. *Int. J. Multiph. Flow* **2000**, *26*, 663–715. [[CrossRef](#)]
37. Fan, L.T.; Ho, T.C.; Walawender, W.P. Measurements of the Rise Velocities of Bubbles, Slugs and Pressure Waves in a Gas-Solid Fluidized Bed Using Pressure Fluctuation Signals. *AIChE J.* **1983**, *29*, 33–39. [[CrossRef](#)]
38. Van der Schaaf, J.; Schouten, J.C.; Johnsson, F. Non-intrusive determination of bubble and slug length scales in fluidized beds by decomposition of the power spectral density of pressure time series. *Int. J. Multiph. Flow* **2002**, *28*, 865–880. [[CrossRef](#)]
39. Grace, J.R.; Bi, X.; Ellis, N. Chap. 8: Slug Flow. In *Essential of Fluidization Technology*; John Wiley & Sons Ltd.: Chichester, UK, 2020; pp. 153–162.
40. Plancherel, M.; Leffler, M. Contribution à l'Etude de la Représentation d'une Fonction Arbitraire par des Intégrales Définies. *Rend. Circ. Mat. Palermo* **1981**, *30*, 289–335.